Cell type-specific inhibitory modulation of sound processing in the auditory thalamus.

Rolón-Martínez, S[1]., Mendoza, A.J.[2], Angeloni, C.F.[1], Vogler, N.W.[1], Chen, R.[1], Vu, K.[2], Haas, J.S.[2#], Geffen M.N.[1#] *

[1]*Department of Otorhinolaryngology, University of Pennsylvania, Philadelphia, PA, United States*

[2]*Department of Biological Sciences, Lehigh University, Bethlehem, PA, United States*

 # These authors contributed equally.

*Corresponding author:
Maria Neimark Geffen, Ph.D. (she/her)
Department of Otorhinolaryngology
Perelman School of Medicine
University of Pennsylvania
5 Ravdin
3400 Spruce St.
Philadelphia PA 19104
Tel.: 215.898.0782

Julie S. Haas
Department of Biological Sciences
Lehigh University
111 Research Drive, Bethlehem PA 18015
610-758-6276

ABSTRACT

Inhibition plays an important role in controlling the flow and processing of auditory information throughout the central auditory pathway, yet how inhibition shapes auditory processing in the medial geniculate body (MGB), the key region in the auditory thalamus, is poorly understood. MGB gates the flow of auditory information to the auditory cortex, and it is inhibited largely by the thalamic reticular nucleus (TRN). The TRN comprises two major classes of inhibitory neurons: parvalbumin (PV^{TRN})-positive and somatostatin (SST^{TRN})-positive neurons. PV and SST neurons have been shown to play differential roles in controlling sound responses in other brain regions. In the somatosensory and visual subregions of the TRN, PV^{TRN} and SST^{TRN} neurons exhibit anatomical and functional differences. However, it remains unknown whether and how PV^{TRN} and SST^{TRN} neurons differ in their anatomical projections from the TRN, and whether and how they differentially modulate activity in the vMGB. We find that PV^{TRN} and SST^{TRN} neurons exhibit differential projection patterns within the thalamus: PV^{TRN} neurons predominantly project to vMGB, whereas SST^{TRN} neurons project to the dorso-medial regions of MGB. Furthermore, PV^{TRN} and SST^{TRN} neurons bi-directionally modulate sound responses in MGB. Selective optogenetic inactivation of PV^{TRN} neurons increased sound-evoked activity in over a third of MGB neurons, while another large fraction of neurons showed suppressed activity. In contrast,

inactivating SST^{TRN} neurons largely reduced tone-evoked activity in vMGB neurons. Cell type-specific computational models identified candidate circuit mechanisms for generating the bi-directional effects of TRN inactivation on MGB sound responses. These distinct inhibitory pathways within the auditory thalamus reveal a cell type-specific role for thalamic inhibition in auditory computation.

INTRODUCTION

Inhibition is crucial to sensory information processing and transmission in the brain. In the auditory system, inhibition plays a critical role in shaping auditory computations, from sound localization in the brainstem to statistical inference in the auditory cortex[1–7]. There are many different inhibitory neuron types within the central auditory pathway which differ morphologically, electrophysiologically, and functionally. In auditory cortex, two major sub-classes of inhibitory neurons, parvalbumin- (PV) and somatostatin- (SST) positive neurons, play distinct functional roles[8–16], and activating PV or SST neurons leads to a decrease in frequency selectivity and an overall increase in tone responsiveness of cortical excitatory neurons[10,13,17,18]. SST, but not PV, neurons contribute to stimulus-specific adaptation, a phenomenon in which neurons adapt selectively to a subset of inputs presented frequently[8,9,19–23].

However, cortical neurons are not the only cells that receive targeted inhibition along the auditory pathway. The medial geniculate body (MGB) located within the thalamus receives auditory information from the auditory brainstem, and MGB neurons shape and relay sensory information to auditory cortex[24,25]. This ascending projection from MGB to auditory cortex is shaped by inhibition from the thalamic reticular nucleus (TRN), a thin sheet of inhibitory neurons that targets and envelops the thalamus[26–30]. Anatomically, the TRN receives excitatory collaterals from the MGB as well as from corticothalamic L5 and L6 neurons, and sends feedforward inhibition back to MGB[27,31–35]. Functionally, the TRN filters relevant sensory information important for perception[36–38] and supports optimal behavioral performance in sensory attentional tasks[39–41].

The TRN contains multiple types of inhibitory neurons, predominantly PV and SST positive neurons. Recent findings in TRN subregions dedicated to visual and somatosensory modalities have described segregated distributions of distinct inhibitory neuron subtypes that differentially target distinct thalamic nuclei and exhibit differences in intrinsic and synaptic properties[42–45]. Thus, it is plausible that as a result of both organizational and functional differences, PV^{TRN} and SST^{TRN} neurons might differentially exert inhibitory control of sound

processing in the MGB. However, the specific roles of PV^{TRN} and SST^{TRN} neurons in gating the auditory thalamocortical relay have not been systematically tested.

In this study, we examined the differential effects of PV^{TRN} and SST^{TRN} neurons on thalamic sound processing. To anatomically identify how PV^{TRN} and SST^{TRN} neurons project to the sub-nuclei of the MGB, we used viral tracing techniques to express an anterograde virus encoding a flexed fluorescent reporter in TRN of transgenic PV-Cre or SST-Cre mouse lines and traced projections to the MGB. We found that PV^{TRN} and SST^{TRN} neurons target distinct subregions of the MGB and differentially modulate neuronal activity. We used viral transfection to drive a soma-targeted inhibitory opsin in the TRN to inactivate PV^{TRN} or SST^{TRN} neurons while recording neuronal activity from neurons in the MGB of awake passively listening head-fixed mice. Inactivating PV cells resulted in a mix of enhanced and suppressed MGB responses. By contrast, inhibiting SST enhanced only a small percentage of MGB responses, but suppressed the vast majority of responses. To identify candidate circuit mechanisms that could underlie the unexpected bidirectional modulation resulting from inactivation of SST^{TRN} and PV^{TRN} neurons, we examined changes in MGB activity in computational models with varied synaptic connectivity within TRN and from TRN to MGB. These simulations revealed several variations of underappreciated thalamic circuitry that can explain the experimental results, including disynaptic inhibition and underappreciated divergent inhibition. Together, our results demonstrate cell and circuit specificity of inhibition within the auditory thalamus that is likely to influence auditory perception.

MATERIALS AND METHODS

Animals.

We performed all experimental procedures in accordance with NIH guidelines on use and care of laboratory animals and by approval of the Institutional Animal Care and Use Committee at the University of Pennsylvania (protocol number 803266). Care was taken to minimize any pain, discomfort, or distress of the animals during and following experiments. Experiments were performed in adult male (n = 12) and female (n = 12) mice aged 3-8 months and weighing 20-32g. The mouse lines used in this study were crosses between Cdh23 mice (B6.CAST-$Cdh23^{Ahl+}$/Kjn; RRID:IMSR_JAX:002756)—a transgenic line that has a targeted point reversion in the Cdh23 gene which protects mice from age-related hearing loss[46]—and PV-Cre mice (B6.129P2-$Pvalb^{tm1(cre)Arbr}$/J; RRID:IMSR_JAX:017320) or SST-Cre mice ($SST^{tm2.1(cre)Zjh}$/J; RRID:IMSR_JAX:013044). Mice were housed at 28°C on a reversed 12hr light-dark cycle with ad libitum access to food and water. Experiments

were performed during the animals' dark cycle and housed individually in an enriched environment after major surgery. Euthanasia was performed by infusion of a ketamine (300mg/kg) and dexmedetomidine (3mg/kg) or prolonged exposure to CO_2. Both methods are consistent with the recommendations of the American Veterinary Medical Association (AVMA) Guidelines on Euthanasia.

Surgical Procedures.

Mice were induced to a surgical plane of anesthesia with 3% isoflurane in oxygen and secured in a stereotaxic frame. Animals were then maintained in an anesthetic plane with 1-2% isoflurane in oxygen and kept at a body temperature of 36°C with the use of a homeothermic blanket. Prior to any surgical procedure, mice were administered subcutaneous injections of sustained release buprenorphine (1mg/kg) for analgesia, dexamethasone (0.2mg/kg) for reduction of swelling, and bupivacaine (2mg/kg), for local anesthesia. Mice received a subcutaneous injection of an antibiotic, enrofloxacin (Baytril; 5mg/kg), for 3 days as part of their post-operative care.

Viral Injections.

Approximately 21 days prior to electrophysiological recordings or transcardial perfusions, we performed small (0.5mm in diameter) unilateral craniotomies using a micromotor drill (Foredom)–under aseptic conditions–over auditory TRN (audTRN) or MGB. Glass syringes attached to a syringe pump (Pump 11 Elite, Harvard Apparatus) were backfilled with modified viral vectors, placed over the brain region of interest, and used to inject virus at 60nL/min. Glass syringes were made using a micropipette puller (P-97, Sutter Instruments) from glass capillaries (Harvard Apparatus, 30-0038) with tip openings ranging from 30μm-40μm in diameter. Following injections, syringes were left in place for 15-20min before retraction. Craniotomies were then covered with bone wax (Fine Science Tools) or a removable silicone plug (Kwik-Cast, World Precision Instruments). The coordinates used to target audTRN were: -1.80mm posterior to bregma, ±2.25mm lateral to bregma, -2.90mm below the pial surface. The MGB coordinates used were: -3.30mm posterior to bregma, ±2.00mm lateral to bregma, -2.90mm below the pial surface. Viral spread was confirmed post-mortem.

Viral Vectors.

For soma-targeted inactivation of PV or SST neurons of the audTRN we injected 400nL of AAV5-hSyn1-SIO-stGtACR1-FusionRed (≥7×10^{12} vg/mL, Addgene 105678-AAV5). For anterograde tracing of PV or SST neurons of the audTRN and control experiments we injected 250nL or 400nL of AAV5-hSyn-DIO-mCherry (≥ 7×10^{12} vg/mL, Addgene 50459-AAV5).

Fiber Optic Cannula & Headpost Implantation.

Following virus injections, fiber optic cannulas (Prizmatix: 3mm in length, 1.25mm in diameter, Ø200µm core, 0.66NA) were implanted above audTRN at a 20° angle, -1.80mm posterior to bregma, ±3.25mm lateral to bregma, and -2.50mm below the pial surface. A small craniotomy was made over the left frontal lobe and a ground pin was implanted. Craniotomies were sealed with Kwik-Cast (World Precision Instruments). The cannula, ground pin and a custom-made stainless-steel headpost (eMachine shop) were then secured with dental cement (C&B Metabond, Parkell) and dental acrylic (Lang Dental).

Tissue Processing.

After allowing time for proper viral expression or following electrophysiological recordings, mice were deeply anesthetized with a cocktail of ketamine and dexmedetomidine (see Animals) and transcardially perfused with 1X PBS followed by 4% paraformaldehyde (PFA) in PBS. Brains were extracted and post-fixed in 4% PFA overnight at 4°C. Following post-fixation, tissue was cryoprotected in 30% sucrose for at least 24hrs at 4°C until sectioning. Brain sections of 40µm-50µm in thickness were cut on a cryostat (Leica CM1860) and collected for immunohistochemistry or imaging of viral expression. For imaging of viral expression or probe location, 50µm-thick sections were mounted on gelatin-coated glass slides and coverslipped using ProLong Diamond Antifade Mounting media with DAPI (Catalog # P36971, Invitrogen). For immunohistochemistry, 40µm-thick sections were collected in 12-well plates filled with 1X PBS (~5-10 sections per well). Slides were imaged using a fluorescent microscope (Leica DM6 B) or a confocal microscope (Zeiss LSM 800).

Immunohistochemistry.

Free-floating 40µm-thick brain sections were first washed in 1X PBS (3 x 10min washes). To increase membrane permeability, sections were microwaved for approximately 10 seconds and then incubated in a solution of 0.3% Triton X-100 in 1X PBS (hereinafter referred to as PBT) for 30 min at room temperature. The

sections were then incubated in a blocking solution consisting of 5% normal goat serum in PBT (hereinafter referred to as PBTG) for 30min-1hr at room temperature. Following incubation with PBTG, sections were incubated in primary antibody solution which consisted of the following antibodies diluted in PBTG: (1) 1:500 mouse monoclonal anti-Parvalbumin (Swant, PV-235; RRID:AB_10000343), (2) 1:500 rabbit polyclonal anti-Somatostatin (Immunostar, 20067); RRID: AB_572264), and (3) 1:1000 rabbit polyclonal anti-Calretinin (Swant, Calretinin-7697; RRID:AB_2721226). Incubation in primary solution was done overnight-48hrs at 4°C on a shaker (Fisher Scientific); well plates were covered with parafilm and a plastic lid. Following the incubation period with primary antibody solution, sections were washed in PBT (3 x 10min washes). Sections were then incubated in secondary antibodies conjugated to fluorescent markers diluted in PBTG for 2hrs at room temperature; well plates were covered with aluminum foil to block light. Secondary antibodies used were: (1) Alexa Fluor Plus 488 Goat anti-Mouse IgG (H+L) (for PV stain; catalog # A32723, Invitrogen; RRID: AB_2633275), (2) Alexa Fluor Plus 488 Goat anti-Rat IgG (H+L) (for SST stain; Catalog # A48262, Invitrogen; RRID: AB_2896330), and (2) Alexa Fluor Plus 488 Goat anti-Rabbit IgG (H+L) (for Calretinin stain; Catalog # A32731, Invitrogen; RRID: AB_2633280). Sections were then incubated for 10min in a 1:40,000 dilution of DAPI stock solution in PBT (5mg/mL, Invitrogen; D1306). The sections were subsequently washed in 1X PBS (5 x 10min washes). Sections were then mounted on gelatin-coated glass slides, coverslipped using ProLong Diamond Antifade Mounting media (Catalog # P36970, Invitrogen) and left to curate in the dark, on a flat surface at room temperature for at least 24hrs prior to imaging. Slides were imaged using a fluorescent microscope (Leica DM6 B) or a confocal microscope (Zeiss LSM 800).

Acoustic Stimuli.

Stimuli were generated using custom MATLAB code and were sampled at 200kHz with a 32-bit resolution. Acoustic stimuli were delivered through a speaker (Multicomp by Newark, MCPCT-G5100-4139) positioned in the direction of the animals' ear contralateral to the recording site. To assess stimulus-locked auditory responses, we used a set of click trains made up of 5 broadband noise bursts at a rate of 1Hz. The noise bursts were 25ms long and presented at a rate of 10Hz for a total of 500ms. To assess frequency response functions in neuronal population, we generated a set of 19 pure tones of logarithmically spaced frequencies ranging between 3kHz and 80kHz at 70dB sound pressure level relative to 20μPa (SPL). Each tone was 50ms long with a 1ms cosine squared ramp, repeated 40 times with an inter-stimulus-interval of 300ms and presented

in a pseudo-random order. 20 of those 40 tone repetitions were accompanied by a continuous light pulse with a 1ms cosine squared ramp starting at tone onset and ending at tone offset (50ms long; for details on light stimuli see Optogenetic Inactivation).

Optogenetic Inactivation and Calibration.

To inactivate populations of neurons, we injected a soma-targeted inhibitory opsin in the audTRN of PV- and SST-Cre mice (see Viral Injections and Viral Vectors). Light-only recordings were achieved by delivering continuous (1ms cosine squared ramp) light pulses of different durations (10ms, 25ms, 50ms, and 100ms) through an implanted fiber-optic cannula via a fiber-coupled blue LED (460nm, Prizmatix, Optogenetics-LED-Blue). Frequency tuning Light_{On} trials were achieved by delivering a continuous 50ms pulse with a 1ms squared ramp.

To reduce variability in the effects of optogenetic manipulation across mice, we developed a procedure to calibrate the LED source prior to each recording session. Once the probe was in its final depth for recording, we presented alternating click trains (see Acoustic Stimuli) wherein each trial consisted of a click train without LED stimulation followed by a click train paired with LED stimulation with 20 different intensities (LED driving voltage ranged from 0 to 5V) while recording neural responses. This stimulus set was presented 10 times for each intensity value. Neural responses were sorted offline using Kilosort2. To calculate if each unit was significantly sound responsive and discard noise clusters, we computed a Wilcoxon sign-rank test between the sound responses during the LED-off click trains and a baseline period of activity. Excluded units from further analysis are those whose P-values exceeded a Bonferroni-corrected α-level of $0.05/n_{\text{clusters}}$. We then calculated the number of spikes during the LED_{off} click train trials (n_{OFF}) and during the LED_{on} click train trials (n_{ON}) and computed the percent change in the response (r_{PC}) for each light intensity:

$$r_{\text{PC}} = \frac{n_{\text{ON}} - n_{\text{OFF}}}{n_{\text{OFF}}} * 100$$

Using a logistic function, we fit the response function as a function of the LED voltage,

$$y = a + \frac{b}{1 + e^{-(x-c)d}}$$

where a determines the y-offset of the response, b determines the range of the response, c determines the x-offset, and d determines the gain of the response. With this fit equation, we found the voltage values that elicited a 100% increase (2-fold change) in neural spiking and used that value for the rest of the stimulus presented in

each individual recording session (0.1-5mW). Some sessions did not show a 2-fold increase with LED manipulation; for these sessions we used maximum LED power (5mW) for all stimuli.

Acute Electrophysiological Recordings.

All electrophysiological recordings were carried out in a double-walled acoustic-isolation booth (Industrial Acoustics). At least 21 days post-viral injection, animals were anesthetized (see Surgical Procedures) and a small craniotomy (1mm in diameter) was performed using a micromotor drill (Foredom) over MGB (for coordinates see Viral Injections). Mice were then clamped into a custom base and allowed to recover from anesthesia for at least 30min. Following their recovery time, we vertically (0° on stereotaxic arm) lowered a 32-channel silicon probe (NeuroNexus: A1x32-Poly2-10mm-50s-177) to a depth of ~3.5mm from the pial surface using a motorized micromanipulator (Scientifica) attached to a stereotaxic arm (Kopf) at a rate of 1-2μm/s. While we lowered the probe, a train of brief broadband noise clicks were played (see Acoustic Stimuli), if we observed stimulus-locked responses, we determined the probe was in a sound-responsive area. The probe was coated in lipophilic far-red dye (Vybrant DiD, Invitrogen), to determine recording sites post-hoc (see Tissue Processing; Figure 2C). Recordings that did not display stimulus-locked responses or were not determined to be in MGB were not used in this analysis. Once the probe reached the target recording depth, it was left to settle in the brain for at least 30min prior to recording. Neural signals were amplified via an Intan headstage (RHD 32ch, Intan Technologies), recorded at a rate of 30kHz using an OpenEphys acquisition board and GUI[47], and digitized with an SPI cable. Signals were filtered between 500 and 6000Hz, offset corrected, and re-referenced to the median of all active channels. Recorded neural data were spike sorted using KiloSort2[48] and manually corrected using phy2. Upon manual correction, units were classified as either single- or multi- units; if units exhibited a clear refractory period, they were labeled single units, otherwise they were classified as multi-units. Both single-units and multi-units were included in all analyses (for number of units used see Table 1). Approximately 3 recording sessions were achieved from each individual mouse at different recording sites.

Gray Value Analysis & Cell Counting.

Gray Value: We first delineated the MGB across the different ROI's. We then used Fiji's Plot Profile plug-in to output the gray values. Using a custom Python script we then calculated the mean gray values and S.E.M.

Cell Counting: We used the Cellpose[49] anatomical segmentation algorithm to outline cells in selected sections. We then manually confirmed the masks provided by Cellpose in Fiji using the cell counter plugin. A custom Python script was used to calculate the overlapping masks and percentages.

Neural Response Analysis.

Following manual spike sorting, units included in this analysis were selected based on their sound responsive profiles. To select sound-responsive units, we used the find_peaks function from SciPy's Python Library and set the minimum peak height to the mean of the baseline activity–calculated as the average firing rate 50ms prior to tone onset ±3 standard deviations of each unit. If units did not display peaks above this set criteria during the presentation of the tone in light-Off conditions, they were labeled as non-sound responsive units and excluded from further analysis. Spontaneous firing rate was computed as the average firing rate during a time window of 50ms prior to tone onset ($FR_{Spontaneous}$) for both light-Off and light-On trials. Tone-evoked firing rate (FR_{Evoked}) was calculated as the average firing rate for the first 25ms (0-25ms) of the total tone duration (50ms). Late tone-evoked firing rate was calculated ($FR_{EvokedLate}$) was calculated as the average firing rate from 25ms to tone offset (25ms-50ms). Offset responses (FR_{Offset}) were calculated as the average firing rate during a 150ms time-window after tone offset. Light only responses were calculated as the average firing rate during light presentation. We calculated the difference in the response between light-Off and light-On conditions by subtracting the mean normalized firing rate during the first 25ms of tone presentation in the light-Off trials and the mean normalized firing rate during the first 25ms of tone presentation in the light-On trials. To calculate frequency response functions, we averaged the firing rate during early-tone presentation (0-25ms) for all the trials of the individual 19 frequencies in both light-Off and light-On conditions and centered them to their best frequency. Best frequency is defined as the frequency that elicited the highest change in firing rate compared to baseline activity. Linear fits were calculated by using SciKit Learns Linear Regression Model (Python Library) on the mean firing rate of each cell for every repeat of each of the 19 frequencies. Using the outputs of this model, we extracted the slope and the y-intercepts of the fit for each unit's frequency response function.

Statistical Analysis.

We assessed normality of the data using a Shapiro-Wilk tests using Scipy's Stats Python Library. For paired data that violated the assumption of normality, p values were calculated using a Wilcoxon sign-rank tests

using Scipy's Stats Python Library. For non-paired data that violated the assumption of normality, p values were calculated using a Wilcoxon rank-sum tests using Scipy's Stats Python Library. The standard error of the mean was used to calculate error bars (±SEM). Symbols: * indicates p values <0.05, ** indicates p values < 0.01, and *** indicates p values <0.001.

Modeling.

Model cells were Hodgkin-Huxley formalism solved by a second order Runge-Kutta ODE solver in MATLAB (ode23, Mathworks). TRN and MGB cells were single-compartment Hodgkin-Huxley models built upon those used previously [50–52] that include T currents. To match the reduced bursting properties in SST^{TRN} and higher-order MGB cells[43,53], those cells had 50% reduced T current densities (0.375 mS/cm²). Parameters included the following ionic currents and maximal conductances: fast transient Na+ (NaT) 60.5 mS/cm², K+ delayed rectifier (Kd) 60 mS/cm², K+ transient A (Kt) 5 mS/cm², slowly inactivating K+ (K2) 0.5 mS/cm², slow anomalous rectifier (AR) 0.025 mS/cm², and low threshold transient Ca2+ (CaT) 0.75 mS/cm² for PV/MGB cells and 0.375 mS/cm² for SST/HO cells. Reversal potentials were 50 mV for sodium, -100 mV for potassium, 125 mV for calcium, -40 mV for AR and -75 mV for leak. Capacitance was 1 μF/cm² with leak of 0.1 mS/cm². Chemical synapses were modelled as double exponential decay with rise and fall time kinetics of 5 ms and 35 ms respectively, with reversal potentials of 0 mV for excitatory and -100 mV for inhibitory synapses. Electrical synapses were modelled as static coupling conductance of 0.03 mS/cm² applied to the voltage difference between the coupled TRN cells, corresponding to a strong electrical coupling (~0.2 coupling coefficient). Tone inputs were simulated as exponentially decaying current pulses (peak amplitude 2.7 μA/cm², with decay time constant 30 ms) delivered simultaneously to each of the MGB cells. Each of the TRN cells was inactivated individually through a static conductance of 10 mS/cm² and reversal potential of -70 mV for 100 ms during the inputs (**Figure 6B**). Chemical synaptic connections between TRN cells were set at 1 μA/cm² for excitatory synapses from MGB to TRN cells, and 3 μA/cm² for all inhibitory synapses originating from TRN. For each stimulus condition, we repeated 150 trials under Poisson random noise of 0.2 μA at a rate of 80 Hz for excitatory and 20 Hz for inhibitory events. Among these trials, we varied the percent of trials that included various synaptic connections from TRN cells (**Figure 6C**), in lieu of varying synaptic strengths. Subthreshold current steps of 0.3 μA were applied to all cells to increase excitability. PSTHs were obtained from spike time data histograms with

a bin size of 1 ms and smoothed with a 31 ms Hanning window. We normalized each response to the maximum rate in the non-inactivated trial.

RESULTS

PV and SST neurons of the TRN project to MGB, targeting different subregions.

MGB is anatomically subdivided into three main subnuclei: the ventral division (vMGB), the medial division (mMGB), and the dorsal division (dMGB). vMGB receives lemniscal projections from the brainstem and provides the most direct auditory input to auditory cortex (AC), whereas dorso-medial geniculate regions provide higher-order information. We first imaged the distribution of PV^{TRN} and SST^{TRN} neuronal projections in MGB using viral neuroanatomical tracing methods. We injected anterograde adeno-associated viruses into the TRN of PV-Cre or SST-Cre mice and traced the axonal projections to the MGB (**Figure 1A & 1C**). We took advantage of the finding that calretinin is solely expressed in the higher-order MGB[54] to characterize the projection patterns of both neuronal subtypes within the MGB. We labeled cell bodies in dorso-medial MGB using calretinin anti-body. The anterograde virus labeled axons in MGB from PV^{TRN} or SST^{TRN} neurons. Whereas PV^{TRN} neurons targeted the central portion of vMGB, SST^{TRN} neurons avoided this region. PV^{TRN} projections were stronger in the central area of ventral MGB rather than peripheral and dorso-medial regions (**Figure 1B;** *$N = 14$ ROIs, $p \leq 0.001$, signed-rank test*). By contrast, projections of SST^{TRN} targeted the dorsal and medial MGB (**Figure 1D;** *$N = 8$ ROIs, $p = .023$, signed-rank test*). Combined, these data demonstrate that PV^{TRN} and SST^{TRN} neurons exhibit differential projection patterns to the MGB.

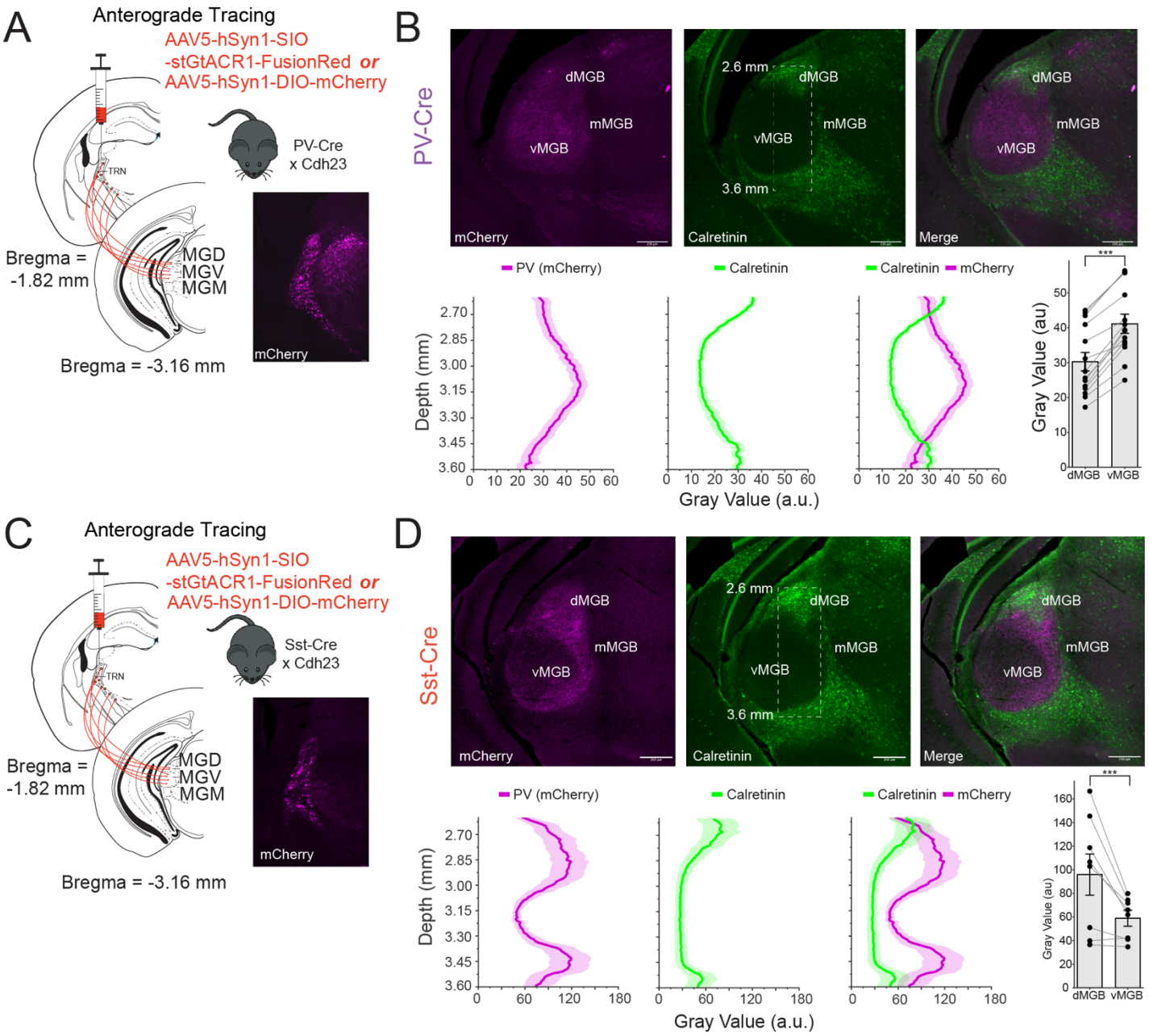

Figure 1. PV^{TRN} and SST^{TRN} project to different subregions of the MGB. A. Experimental design for anatomical experiments. PV-cre mice were injected with AAV5-hSyn1-DIO-mCherry into TRN for anterograde tracing of PV neurons in the TRN. Inset: mCherry expression in the TRN indicating the localization of the virus. **B. Top**: Projections of PV^{TRN} neurons primarily target the ventral subdivision of the MGB. *Left panel*: Viral expression of projections to the MGB (magenta). *Middle panel*: Immunohistochemical labeling of calretinin in the MGB (green). *Right panel*: Merged channels. **Bottom**: Quantification of the fluorescence intensity of projections from PV^{TRN} neurons that target MGB (Dashed box in top middle panel outlining the ROI). *Left panel*: intensity of viral expression of projections to the MGB in the ROI along the dorso-ventral axis. Dashed lines indicate extent of vMGB. *Middle panel*: intensity of the immunohistochemical labeling of calretinin in the MGB in the ROI along the dorso-ventral axis. *Right panel*: merged channels. *Barplot:* mean intensity of the projections of PV-audTRN neurons in dorsal and ventral MGB (N =14 ROIs; n = 3 mice). **C.** SST-cre mice were injected with AAV5-hSyn1-DIO-mCherry into TRN for anterograde tracing of SST neurons in the TRN. **D. Top**: Projections of SST^{TRN} neurons primarily avoid the ventral subdivision of the MGB. *Left panel*: Viral expression of projections to the MGB (magenta). *Middle panel*: Immunohistochemical labeling of calretinin in the MGB (green). *Right panel*: Merged channels. **Bottom**: Quantification of the fluorescence intensity of projections from SST^{TRN} neurons that target MGB (Dashed box in top middle panel outlining the ROI). *Left panel*: intensity of viral expression of projections to the MGB in the ROI along the dorso-ventral axis. *Middle panel*: intensity of the

immunohistochemical labeling of calretinin in the MGB in the ROI along the dorso-ventral axis. *Right panel*: merged channels. *Barplot:* mean intensity of the projections of PV-audTRN neurons in dorsal and ventral MGB (N =8 ROIs; n = 3 mice). *Scale bar = 0.25 mm. vMGB: ventral MGB; dMGB: dorsal MGB; mMGB: medial MGB; White dashed box in the top middle panel indicates ROI for fluorescence intensity quantification.*

Inactivation of PV^{TRN} and SST^{TRN} neurons differentially affects tone-evoked responses in the MGB.

Because of our anatomical results and previous work identifying genetically distinct TRN neurons that express different anatomical and physiological properties[42,43], we next tested whether and how MGB neurons are modulated by PV^{TRN} and SST^{TRN} neurons. We inactivated SST and PV neurons in audTRN during tone-evoked responses in MGB neurons. We injected a Cre-dependent soma-targeted inhibitory opsin (AAV5-hSyn-SIO-stGtACR1-FusionRed) in the audTRN of SST-Cre or PV-Cre mice (**Figure 2A-B, 2G-H**). This virus only expresses in the soma of Cre-expressing neurons, reducing the chance of effects from backpropagating action potentials from local terminals[55]. We verified that the virus expression was restricted to the appropriate cell type (**Supplementary Figure S1**). We then implanted an optic fiber above audTRN, a headpost, and a ground pin for awake *in-vivo* electrophysiological recordings. In our experiments, mice passively listened to tones ranging from 3-80kHz, while we recorded and measured the spiking activity of MGB neurons. We quantified neuronal firing rate for both light-off and light-on conditions and calculated the difference between these conditions as a function of probe depth within the MGB (**Figure 2D-F, 2I-K**). To confirm that our optogenetic manipulations indeed inhibited audTRN neurons, in a separate set of experiments, shining light over the TRN suppressed tone-evoked neuronal activity in neurons recorded in TRN (**Supplementary Figure S2**). We have separately verified in slices that shining light over the TRN resulted in silencing of a neuron expressing stGtACR1 (**Supplementary Figure S3**).

We expected that PV^{TRN} neuronal inactivation would drive the disinhibition of responses of MGB neurons, which would be stronger in the central vMGB. By contrast, we expected that inactivating SST^{TRN} neurons would suppress MGB responses to sounds via a double inhibitory pathway. Because SST^{TRN} and PV^{TRN} are reciprocally connected, inactivating SSTs could disinhibit PVs which would in turn suppress MGB neurons. This effect would be stronger in the central regions of MGB, and there would be mixed effects in the dorsal regions of the MGB.

Indeed, inhibiting PV^{TRN} neurons facilitated sound-evoked responses in a large fraction of MGB neurons (**Figure 2D-F**). The facilitation was stronger for the central regions of MGB than dorsal MGB ($p = 0.0070$,

binned by depth: 2.5-2.9mm versus 3.1-3.5 mm, rank-sum test), and this change was exacerbated by the larger number of facilitated neurons in center (**Figure 2F**). Surprisingly, there was also a strong suppression of a fraction of neurons throughout MGB. However, this suppression was not differential across the depth of MGB (p = *0.18, rank-sum test)*. Inactivating SST^{TRN} neurons resulted in a dominant suppression of tone-evoked responses in MGB, with a handful of neurons exhibiting facilitation (**Figure 2I-K**). Furthermore, the suppression was stronger in the dorsal MGB as compared to vMGB (p = *0.000050, rank-sum test*). These results suggest that PV neurons provide direct inhibition to MGB, while SST neurons disinhibit the thalamocortical auditory pathway.

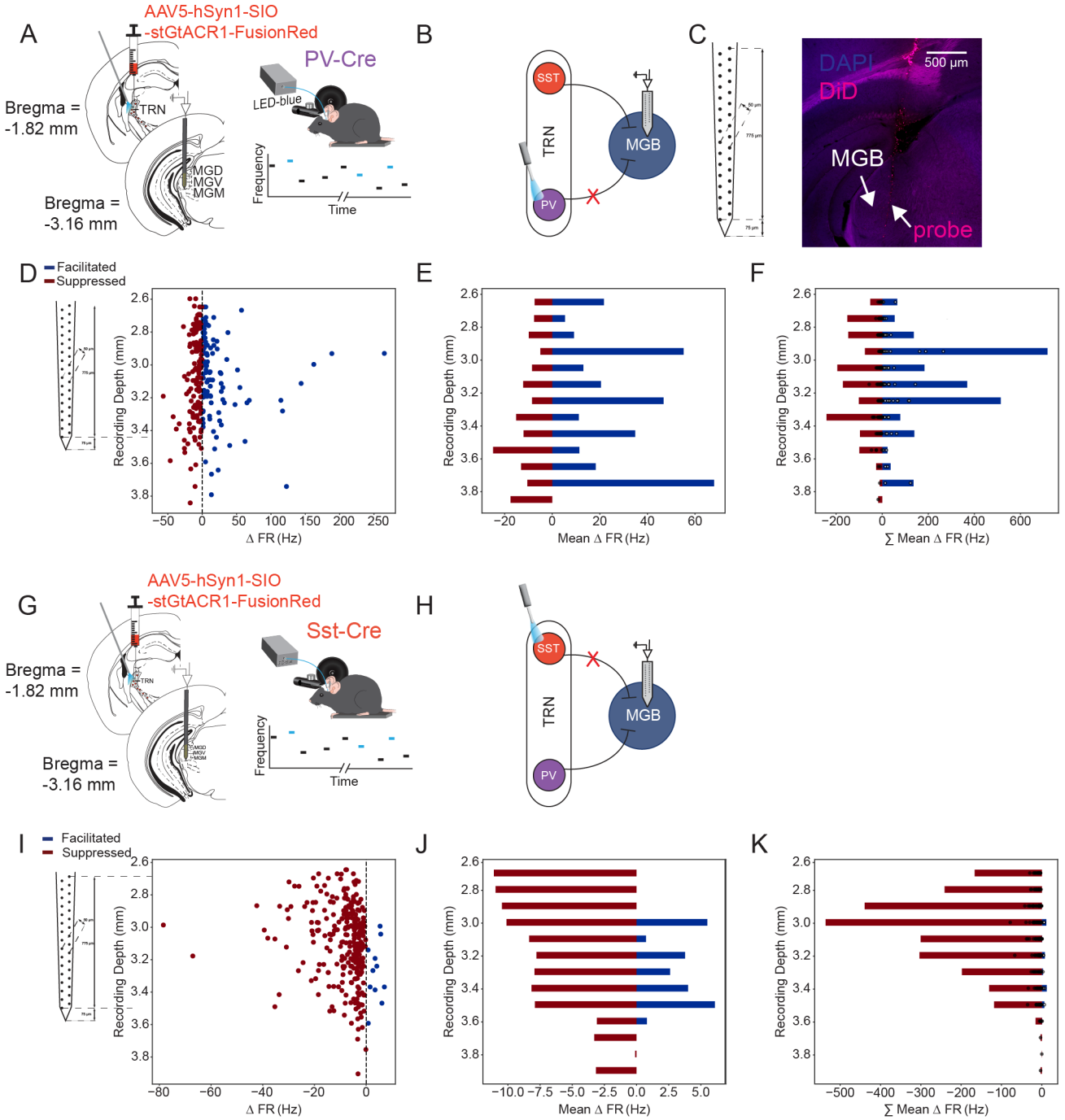

Figure 2. Inactivation of PV^{TRN} and SST^{TRN} neurons differentially affect tone-evoked activity in MGB neurons. A. PV mice were injected with a soma-targeted AAV5-hSyn1-DIO-stGtACR1-FusionRed into the audTRN and were implanted with an optic fiber. We recorded from MGB neurons in awake head-fixed mice. We presented a set of pure tones in light-on and light-off conditions. **B.** We selectively inactivated PV neurons of the audTRN while recording from neurons in the MGB using a vertical multi-channel electrode that spanned the depth of dMGB and vMGB, with the top electrode positioned at the tip of dMGB. **C.** Example probe track labeled using DiD (magenta), from a recording in MGB. **D.** Scatter plot showing the change in firing rate (FR) of recorded MGB neurons with PV^{TRN} inactivation as a function of probe depth. Red: suppressed neurons; Blue: facilitated neurons. **E.** Mean change in FR of recorded MGB neurons with PV^{TRN} inactivation as a function of probe depth in 100 µm bins. **F.** Total change in FR of recorded MGB neurons with PV^{TRN} inactivation as a function of probe depth in 100 µm bins. **G-K.** Same as **A-B, D-F**, but for SST^{TRN}

inactivation. (N (PV) =239, n = 4 mice. N (SST): 282, n = 4 mice). ROIs; n = 3 mice). *Scale bar = 0.25 mm. vMGB: ventral MGB; dMGB: dorsal MGB; mMGB: medial MGB; White dashed box in the top middle panel indicates ROI for fluorescence intensity quantification.*

Inactivation of PV^{TRN} neurons facilitates or suppresses tone-evoked responses in MGB.

We next examined in more detail the effect of inactivating PV^{TRN} neurons on tone-evoked responses in MGB. For a representative *facilitated* MGB neuron, the raster plots and peri-stimulus time histogram (PSTH) (**Figure 3A-B**) demonstrate an increase in activity during tone presentation. For this neuron, the increase was more pronounced 0-25 ms after stimulus onset and affected the responses across tone frequencies (**Figure 3C**). The effects subsided 25-50 ms after stimulus onset (**Figure 3D**). For a representative *suppressed* MGB neuron, the raster plot and PSTH depict a reduction in spiking activity during the tone (**Figure 3E-F**). The suppressive effects of PV^{TRN} inactivation were more pronounced 0-25 ms (**Figure 3G**) but persisted 25-50 ms after tone onset (**Figure 3H**).

Across the population of MGB neurons, during tone presentation, 35% of neurons were facilitated, 48% of neurons were suppressed and 17% of neurons in the MGB were not affected due to PV^{TRN} inactivation (**Figure 3I**). Facilitated neurons demonstrated a sharp peak followed by a prolonged decay in firing rate after tone onset and in the absence of a tone (**Figure 3J**). Similarly, for suppressed neurons, the effect of the light in the absence of tone was prolonged, and with tone resulted in an overall decrease in peak tone-evoked response followed by a reduction in activity (**Figure 3K**). Over the population, there was no significant effect during spontaneous activity prior to sound and light stimulus on no-light and light-on trials (**Figure 3M**). In the tone condition, neuronal activity was significantly facilitated or suppressed both in the beginning (0-25 ms) and during the second half (25-50 ms) of the tone duration (**Figure 3N-O;** *N (facilitated): 101, N (suppressed): 138; p (facilitated-0-25ms) ≤ 0.001, p (suppressed-0-25ms) ≤ 0.001; p (facilitated-25-50ms) ≤ 0.001, p (suppressed-25-50ms) ≤ 0.001; signed-rank test*). When PV^{TRN} neurons were inactivated, time-to-peak significantly increased in the facilitated MGB neurons and slightly decreased in the suppressed MGB neurons (**Figure 3L;** *N (facilitated): 101, N (suppressed): 138; p (facilitated-0-25ms) ≤ 0.001, p (suppressed-0-25ms) ≤ 0.017; signed-rank test*). This suggests that PVs selectively control time-to-peak in neuronal responses in MGB. We confirmed that the light presentation alone did not affect the neuronal firing rate by repeating the experiments after injecting a virus encoding only the fluorescent reporter without the opsin (**Supplementary Figure S4**) and found no effect of light on spontaneous or tone-evoked responses in MGB. Overall, these results demonstrate

that inactivating PV^{TRN} neurons rapidly affected tone-evoked responses in MGB, with effects persisting over the stimulus duration. In addition, we found that PV^{TRN} neurons can both directly suppress neuronal responses in MGB and enhance the response firing rate indicating that these neurons may be involved in multiple mechanisms that shape MGB firing rates.

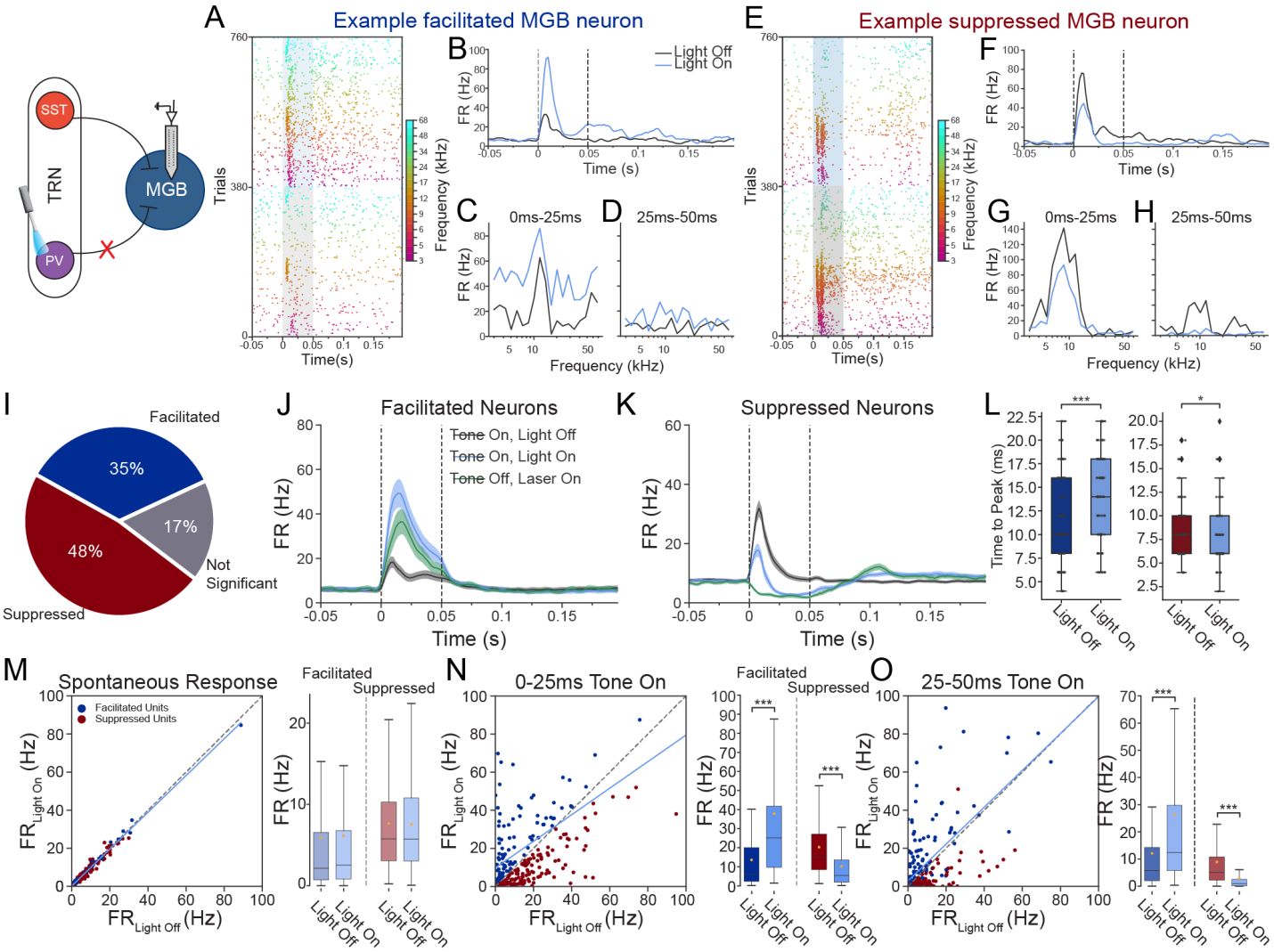

Figure 3. Inactivation of PV^{TRN} neurons facilitates and suppresses tone-evoked activity in MGB neurons. A. PV mice were injected with a soma-targeted AAV5-hSyn1-DIO-stGtACR1-FusionRed into the audTRN and were implanted with an optic fiber. We recorded from MGB neurons in awake head-fixed mice. We presented a set of pure tones in light-on and light-off conditions. We selectively inactivated PV^{TRN} neurons while recording from neurons in MGB. Raster plot of an example facilitated unit; trials are ordered by frequency and light condition. The gray box indicates light off conditions, blue box indicating the light on conditions. **B.** PSTH of the facilitated example unit averaged across all trials for the light off (black line) and light on (blue line) conditions. **C.** Frequency response function for the facilitated unit during the first 25ms of tone presentation during light off and light on conditions. **D.** Frequency response function of the unit during the late 25-50ms of tone presentation. **E-H.** same as A-D, but for a representative facilitated neuron. **I.** Pie chart breaking down the effect of PV^{TRN} inactivation in neurons of the MGB. We find that 48% of recorded units had suppressed tone-evoked responses (red slice), 35% of recorded units had facilitated tone-evoked responses (navy blue slice), and 17% of tone-responsive units were not affected by light manipulation (gray slice). **J,K.** Mean PSTH of facilitated (J) and suppressed (K) recorded neurons in MGB (N = 101 facilitated. N = 138 suppressed). Light-only trials (green line), tone-only trials (black line), and tone- and light-on trials (light blue line). **L.** Time to peak of tone-

evoked responses for facilitated (left, blue) and suppressed (right, red) MGB neurons for light off (blue/red) and light on (light blue) trials. **M-O.** Left: scatter plot, and right: box plot and boxplot of the mean FR for light off and light on conditions for facilitated (blue) and suppressed (red) neurons during spontaneous activity (**M**), 0-25 ms post stimulus onset (**N**), and 25-50 ms post stimulus onset (**O**). N = 239; n = 4. Shaded areas represent SEM±. Error bars represent SEM±. *** denotes p-value < 0.001; * denotes p-value < 0.05.

Inactivation of SST^{TRN} neurons primarily suppresses tone-evoked responses of MGB neurons.

We next examined in more detail the effect of inactivating SST^{TRN} neurons on tone-evoked responses of MGB neurons. For a representative facilitated MGB neuron, the raster plots and post-stimulus time histograms (**Figure 4A-B**) demonstrate an increase in activity at the onset of tone presentation. For this neuron, the increase was present 0-25 ms after stimulus onset and affected the responses to frequencies near the neuron's best frequency (**Figure 4C**). The effects were not apparent in the 25-50 ms tone bin (**Figure 4D**). For a representative suppressed MGB neuron, the raster plot and PSTH depict a reduction in spiking activity throughout the tone (**Figure 4E-F**). The suppressive effects were more pronounced 0-25 ms after tone onset (**Figure 4G-H**).

Across the population of neurons, during tone presentation, 78% neurons were suppressed, only 3% of neurons were facilitated and 19% of neurons in the MGB were not affected by SST^{TRN} inactivation (**Figure 4I**). The average PSTH across the few facilitated neurons (N = 11 neurons) shows barely detectable amplification (**Figure 4J**). For suppressed neurons, suppression driven by SST^{TRN} neuronal inactivation was prolonged in the absence of tone. In the presence of a tone, the tone-evoked response was reduced and shortened (**Figure 4K**). Over the population, there was no significant effect during spontaneous activity on light-on versus light-off trials prior to stimulus (**Figure 4M**). Temporally, neuronal activity was significantly suppressed both in the beginning (0-25 ms) and during the second half (25-50 ms) of the tone presentation (**Figure 4N-O;** *N (facilitated): 11, N (suppressed): 271; p (facilitated-0-25ms) = 0.001, p (suppressed-0-25ms) ≤ 0.001; p (facilitated-25-50ms) ≤ 0.147, p (suppressed-25-50ms) ≤ 0.001; signed-rank test*), although some cells, initially suppressed, exhibited facilitation in the second half of the tone. Unlike for PV^{TRN} suppression, there was no change in the time-to-peak response of facilitated MGB neurons, and a small decrease for suppressed MGB neurons, upon inactivation of SST^{TRN} neurons (**Figure 4L;** *N (facilitated): 11, N (suppressed): 271; p (facilitated-0-25ms) = 0.461, p (suppressed-0-25ms) = 0.003; signed-rank test*). We confirmed that the effects of light presentation alone did not affect the neuronal firing rate by repeating the experiments but injecting a virus encoding only the fluorescent

reporter, and not the opsin (**Supplementary Figure S5**). Overall, these results demonstrate that inactivating SST^{TRN} neurons largely drove a suppression of MGB neurons.

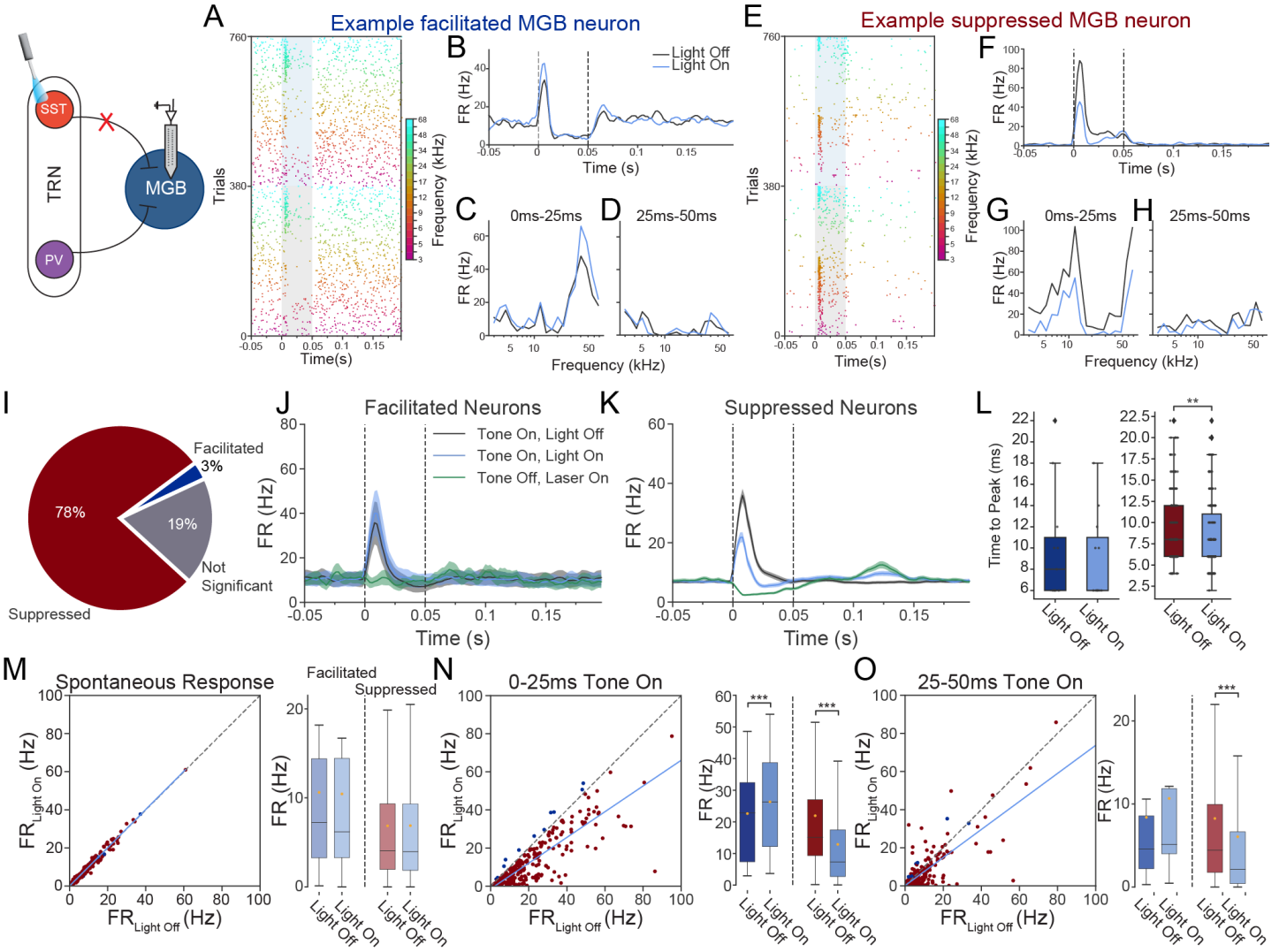

Figure 4. Inactivation of SST^{TRN} neurons predominantly suppresses tone-evoked activity in MGB neurons. A. SST mice were injected with a soma-targeted AAV5-hSyn1-DIO-stGtACR1-FusionRed into the audTRN and were implanted with an optic fiber. We recorded from MGB neurons in awake head-fixed mice. We presented a set of pure tones in light-on and light-off conditions. We selectively inactivated SST^{TRN} neurons while recording from neurons in MGB. Raster plot of an example facilitated unit; trials are ordered by frequency and light condition. The gray box indicates light off conditions, blue box indicating the light on conditions. **B.** PSTH of the facilitated example unit averaged across all trials for the light off (black line) and light on (blue line) conditions. **C.** Frequency response function for the facilitated unit during the first 25ms of tone presentation during light off and light on conditions. **D.** Frequency response function of the unit during the late 25-50ms of tone presentation. **E-H.** same as A-D, but for a representative facilitated neuron. **I.** Pie chart breaking down the effect of SST^{TRN} inactivation in neurons of the MGB. We find that 78% of recorded units had suppressed tone-evoked responses (red slice), 3% of recorded units had facilitated tone-evoked responses (navy blue slice), and 19% of tone-responsive units were not affected by light manipulation (gray slice). **J,K.** Mean PSTH of facilitated (J) and suppressed (K) recorded neurons in MGB (N = 11 facilitated. N = 271 suppressed). Light-only trials (green line), tone-only trials (black line), and tone- and light-on trials (light blue line). **L.** Time to peak of tone-evoked responses for facilitated (left, blue) and suppressed (right, red) MGB neurons for light off (blue/red) and light on (light blue) trials. **M-O.** Left: scatter plot, and right: box plot and boxplot of the mean FR for light off and light on conditions for facilitated (blue) and suppressed (red) neurons during spontaneous activity (**M**), 0-25 ms

post stimulus onset (**N**), and 25-50 ms post stimulus onset (**O**). N = 282; n = 4. Shaded areas represent SEM±. Error bars represent SEM±. *** denotes p-value < 0.001; * denotes p-value < 0.05.

PV^{TRN} and SST^{TRN} differentially affect frequency tuning of MGB neurons.

Inactivation of PV^{TRN} neurons produced significant changes in MGB tuning for both the facilitated- and suppressed-tone evoked activity groups; with a significant shift upwards and a significant shift downwards in the frequency response function, respectively (**Figure 5A-B;** *N (facilitated): 101, N = (suppressed): 138; p (facilitated-all octaves) ≤ 0.001, p (suppressed-all octaves) ≤ 0.001; signed-rank test*). Interestingly, in facilitated MGB neurons, response to best frequency increased less strongly than the response to the sideband frequencies (**Figure 5A;** *N (facilitated) = 101, N (suppressed) = 138; p (facilitated- sidebands) ≤ 0.001, p (facilitated-best frequency) = 0.204; signed-rank test*). To examine frequency selectivity of neurons– or how specific neuronal responses are to a particular frequency–we calculated the sparseness index. A value closer to 1 indicates that the unit responds narrowly to a set of stimuli and a value closer to 0 indicates that units will respond to a broader range of stimuli. We found that inactivation of PV^{TRN} significantly affected sparseness in both subgroups. Following of PV^{TRN} inactivation, sparseness in facilitated MGB neurons significantly decreased, indicating that neurons became more broadly tuned (**Figure 5A;** *N (facilitated): 101; p (both time points) ≤ 0.001; signed-rank test*). Interestingly, in suppressed MGB neurons, PV inactivation increased sparseness, indicating that neurons on average became more narrowly tuned (**Figure 5B;** *N (suppressed): 138; p (both time points) ≤ 0.001; signed-rank test*). These results indicate that of PV^{TRN} neurons contribute to how narrowly or broadly tuned MGB neurons are to auditory stimuli.

Because PV^{TRN} neurons affect frequency tuning of MGB neurons, we asked whether the observed effects of PV^{TRN} inactivation depended on whether the MGB recording site(s) were tonotopically organized along the probe depth (dorsal-ventral axis). To test this, we separately analyzed and compared tonotopic versus non-tonotopic MGB recordings. We found that PV^{TRN} inactivation produced similar effects on MGB sound responses, regardless of recording site tonotopy (**Supplementary Figure S6**).

Inhibition of SST^{TRN} neurons produced no significant changes in tuning for the few MGB neurons that had facilitated tone-evoked responses (**Figure 5C;** *N (facilitated): 11; p (0-25ms) ≥ 0.05; signed-rank test*). However, MGB neurons that had suppressed tone-evoked firing rates show a significant downward shift in the

frequency response function during the first 25ms of the tone presentation and the remaining 25ms of tone presentation (**Figure 5D;** *N = (suppressed): 271; p (both time points) ≤ 0.05; signed-rank test*). We found that inactivation of SST^{TRN} neurons did not affect sparseness in the facilitated group *(***Figure 5C***; N (facilitated): 11; p (0-25ms) = 0.638*; *p (25-50ms) = 0.765*; *signed-rank test*). However, the sparseness index in the suppressed group of neurons was significantly increased during SST^{TRN} inactivation (**Figure 5D;** *N (suppressed): 101; p (both time points) ≤ 0.001; signed-rank test*). Similar to inactivation of PV^{TRN} neurons, we again found that SST^{TRN} inactivation produced similar effects on MGB sound responses, regardless of recording site tonotopy (**Supplementary Figure S7**). Together, these results indicate that SST neurons of the TRN contribute to how narrowly or broadly tuned MGB neurons are to auditory stimuli.

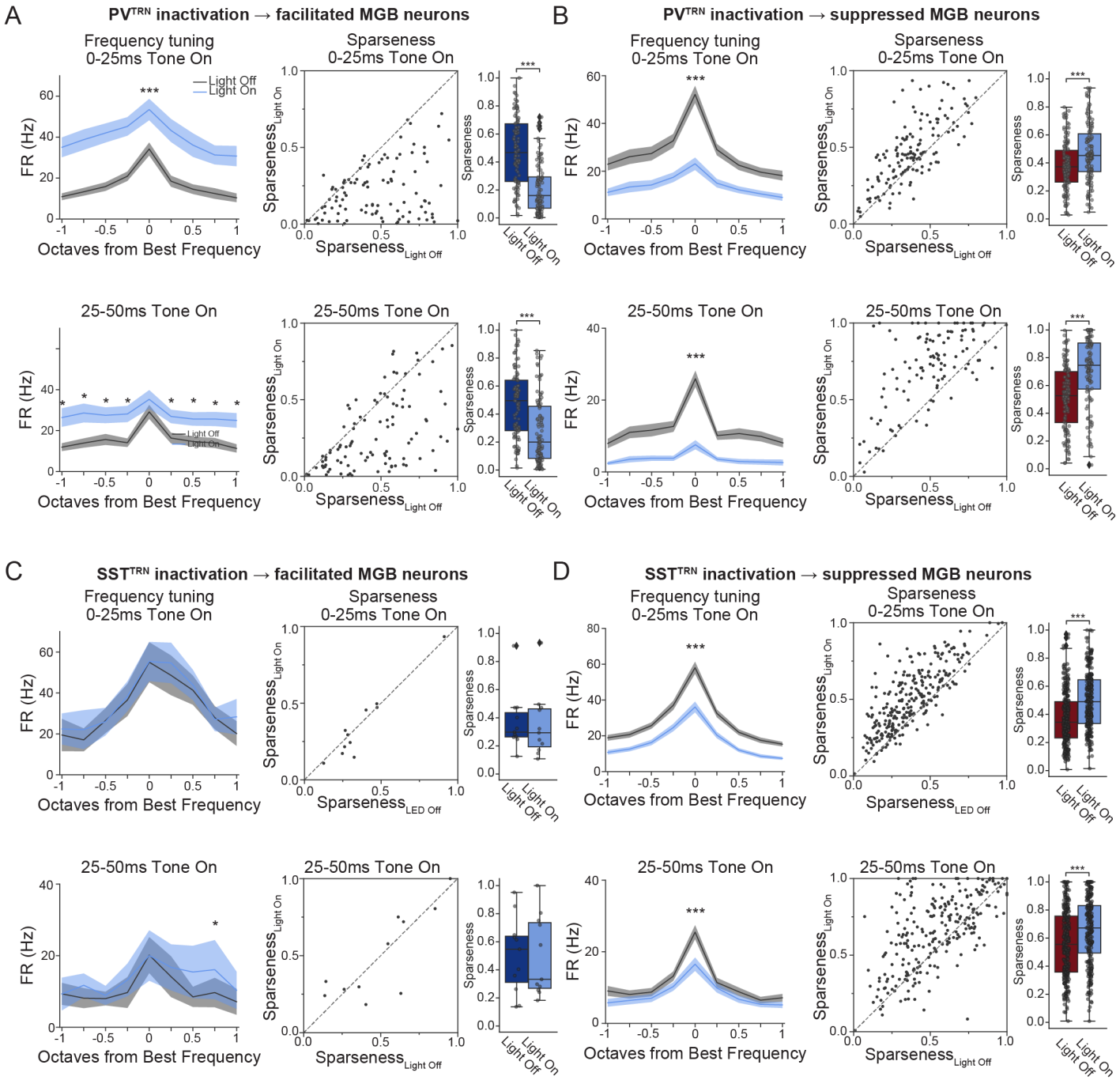

Figure 5. Inactivation of PV^{TRN} and SST^{TRN} neurons differentially affect frequency tuning of MGB neurons. A-D. *Left:* Mean frequency response function for light on (light blue) and light off (light gray) trials for neurons centered on best frequency (0 octaves = BF). Shaded areas represent SEM±. *Right*. Scatterplot and bar plot of sparseness. Error bars represent SEM±. **A, C.** Facilitated neurons. **B, D.** Suppressed neurons. **Top:** 0-25 ms post stimulus onset. **Bottom:** 25-50 ms post stimulus onset. N = 239 neurons; n = 4 mice (PV). N = 282 neurons; n =4 mice (SST). *** denotes p-value < 0.001; * denotes p-value < 0.05.

Specifics of connectivity between MGB-TRN circuits determine the sign of MGB responses during TRN cell-type inactivation.

To examine the many possible connectivity schemes of primary and higher-order auditory thalamocortical circuits that may account for the observed changes in sensory responses during inactivation of specific TRN populations, we constructed a 4-cell Hodgkin-Huxley model (see Methods) comprising two channels: a primary vMGB relay cell reciprocally connected to a PV^{TRN} cell, and a higher-order MGB cell reciprocally connected to a SST^{TRN} cell (**Figure 6A-B**), matching the subtype-specific connections that we identified and have been previously demonstrated for other sensory modalities[42,43]. Without connectivity between primary and higher-order channels, inactivation of the PV^{TRN} cell always allowed substantially increased responses in the vMGB firing rate to a tone input, whereas inhibiting the SST^{TRN} cell has no effect at all on vMGB response, as expected (not shown). Those trials served as a comparison control for subsequent trials.

We first examined whether intra-TRN connectivity would suffice to produce both suppression and facilitation of vMGB responses during cell type-specific silencing (**Figure 3-4**). Electrical synapses extensively couple TRN cells, including coupling between subtypes[45], that may substantially modulate activity within the thalamocortical circuits examined here[51,56]. We examined the effect of inter-type TRN coupling, using a strong electrical synapse with coupling coefficient ~0.2, on the responses of the primary MGB cell. Similar to the uncoupled control case, vMGB responses were facilitated when PV^{TRN} was inactivated (**Figure 6D**, left), and once again as expected we saw no changes in vMGB responses during inactivation of SST^{TRN} (**Figure 6D, right**). Although the existence of inhibitory synapses between TRN neurons in mature tissue has been controversial [57], there is some evidence for lateral inhibition within TRN[58,59]. Inclusion of a lateral inhibitory synapse from SST^{TRN} to PV^{TRN} allowed a facilitated vMGB response during PV^{TRN} inactivation, and we noted that MGB responses during no-inactivation trials were also elevated from the control response (**Figure 6E, left**). Silencing SST^{TRN} cells in this circuit produced a substantial reduction in the tone response of the vMGB neuron compared to control responses (**Figure 6E, right**), matching the experimental results (**Figure 2, 4**) through relief of disynaptic inhibition. Silencing either cell type in a circuit that included inhibitory connections from PV^{TRN} to SST^{TRN} did not reduce tone responses of vMGB, however (not shown). Thus, one specific form of intra-TRN connectivity, from SST^{TRN} to PV^{TRN} cells, is a candidate circuit mechanism underlying the unexpected suppression of MGB during cell type-specific TRN inactivation.

We then asked whether the relative strengths of within-TRN, lateral inhibition and TRN-MGB reciprocal inhibition could control the sign of vMGB responses during selective silencing, as we anticipate that in real tissue, mixes of connectivity and strength will co-exist within a spectrum across these various schemes. To test the effect of heterogeneous circuitry on firing rate changes in primary vMGB cells, we varied the ratio of lateralization within the circuits over a set of trials. In circuits where TRN and MGB are reciprocally connected, varied relative strengths of lateral intra-TRN inhibition always produce facilitation of vMGB responses when PV^{TRN} is inactivated (**Figure 6F, left**); the effect of SST^{TRN} lateralization was only to modulate the total facilitation produced. During SST^{TRN} inactivation, increases in SST^{TRN} lateral inhibition suppressed MGB responses independently of the presence of PV^{TRN} lateral inhibitory synapses (**Figure 6F, top right**). We note that the addition of coupling between TRN cells allowed for bidirectionality in changes in vMGB rate when SST^{TRN} was inactivated, for networks with weak SST-to-PV lateralization (**Figure 6F, bottom right**). From this set of simulations addressing intra-TRN connectivity, we conclude that inactivating SST^{TRN} can reproduce the unexpected suppression of vMGB response when SST-to-PV synapses or gap junctions are included; however, lateral intra-TRN connections alone cannot reproduce the bidirectional effects of PV^{TRN} inactivation.

Next, we asked whether the responses of primary vMGB might change during cell type-specific inactivation in the context of variations in feedback inhibition. TRN cells send divergent inhibitory connections to several MGB cells but often do not send inhibition back to the same cell that excite them[60,61]. Additionally, activation of one thalamic nucleus can produce inhibition in nearby sensory-related nuclei (i.e. activation of POM evoking IPSCs at VPM) thought to arise from TRN[62,63]. Thus, we included and varied the amount of divergent feedback inhibition from TRN to MGB in our circuits. When inactivating PV^{TRN} cells, inclusion of both reciprocal and divergent inhibitory feedback still produced facilitation of the vMGB response (**Figure 6G, left**). For inactivation of SST^{TRN} cells in the context of divergent inhibition, vMGB responses were facilitated when circuits contained both reciprocal and divergent inhibitory synapses (**Figure 6G, right**). In circuits with only divergent but lacking reciprocal inhibitory feedback, PV^{TRN} inactivation produced a suppression of vMGB response (**Figure 6H, left**). Thus, inclusion of divergent feedback is a candidate circuit for reproducing the experimental results of PV^{TRN} inactivation. In circuits with only divergent inhibitory feedback from TRN to MGB cells, SST^{TRN} inactivation produced greater facilitation of vMGB responses (**Figure 6H, right**). Thus, we conclude that uniformly divergent feedback inhibition is unlikely to account for the experimental observations of vMGB suppression during SST^{TRN} inactivation.

Finally, we asked if variations in the relative power of the two types of feedback inhibition, combined, could allow both vMGB enhancement and suppression during cell type-specific inactivation trials. Increasing the relative strength of the divergent inhibitory synapses decreased the responses of the vMGB cell, while increasing the strength of reciprocal inhibition increased those responses, during PV^{TRN} inactivation trials compared to the baseline firing rate (**Figure 6I, top left**). This is consistent with the bidirectionality of the experimental results for PV^{TRN} inactivation (**Figure 3**). SST^{TRN} inactivation produced only increases in vMGB activity, as divergent inhibitory ratio increased from zero (**Figure 6I, top left**), inconsistent with experiments. However, electrical coupling added to this circuitry allowed SST^{TRN} inactivation to diminish vMGB responses for weakly lateralized networks (**Figure 6I, middle**). Including SST^{TRN}-to-PV^{TRN} lateral inhibition in this case modulated the SST^{TRN} inactivation response towards more suppressed outcomes (**Figure 6I, bottom right).** Together, our simulations lead us to conclude that divergent feedback connections, together with electrical synapses or SST^{TRN}-to-PV^{TRN} inhibition, may be embedded within the thalamus and serve as the sources of the bidirectional vMGB responses observed during PV^{TRN} inactivation and the suppression during SST^{TRN} inactivation.

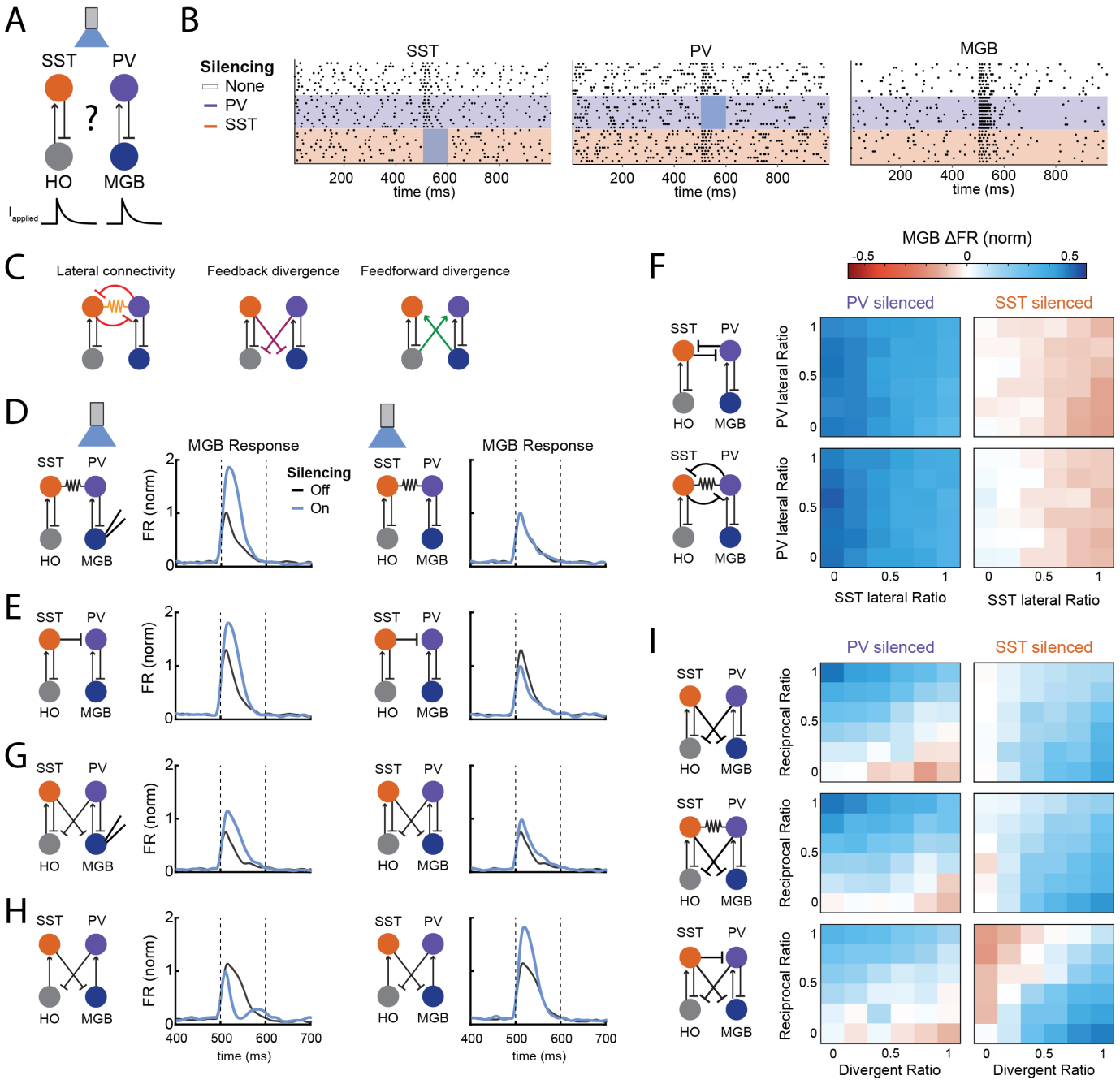

Figure 6. Schemes of circuit connectivity that account for bidirectional modulation of vMGB responses during subtype-specific inactivation in TRN. A. 4-cell model of primary sensory MGB-TRN pairs and higher order (HO) MGB-TRN pairs. **B.** Raster plots from trials with no inactivation, during PV inactivation (purple) and during SST^{TRN} inactivation (orange). **C.** Candidate connectivity schemes tested in models. **D.** PSTH of MGB firing for circuits with electrical coupling between TRN subtypes. MGB responses are normalized to the peak response during non-inactivated trials for no connectivity between columns. Left, primary MGB firing rate to input alone (black line) and with PV^{TRN} silencing (light blue line). Right, MGB firing rate input alone (black line) and with SST^{TRN} silencing (light blue line). **E.** As in D, for a circuit including lateral SST^{TRN} to PV^{TRN} connections. **F**. Effect of inactivation on MGB rate for heterogeneous combinations of lateral inhibitory connections, with and without electrical synapses between TRN cells. The ratio of lateral synapses is the percent of trials that included lateral synapses for each TRN cell type. **G.** As in D, for circuits with both reciprocal and divergent feedback inhibition. **H.** As in D, for circuits containing only divergent inhibition. **I.** Effect of cell type-specific inactivation on MGB rate for heterogeneous inhibitory feedback connections between TRN and thalamic cells. Divergence ratio is the percent of trials that included divergent synapses. Reciprocal ratio is the percent of trials that included reciprocal TRN-MGB synapses. Middle, with electrical coupling between PV and SST cells. Bottom, effect of inactivation on MGB rate with heterogeneous inhibitory connections in addition to lateral inhibition from the SST^{TRN} to PV^{TRN} cells.

DISCUSSION

Differences between intrinsic physiology, synaptic connections, and axonal projections of distinct cell types have been described for the GABAergic neurons of the TRN [42–45], but the impact of those differences on their inhibitory modulation of thalamic processing remains unknown. We used a combination of viral anatomical tracing, optogenetics, and awake *in-vivo* electrophysiological recordings along with computational modeling to study the functional roles of audTRN PV and SST neurons in modulating sound responses in the MGB. Our results confirm that PV and SST neurons project to hierarchically distinct sensory thalamic regions: while PV^{TRN} neurons primarily project to the center of the primary or first-order auditory thalamic sub-region vMGB, SST^{TRN} neurons project almost exclusively to the dorsal subregions of MGB and higher-order auditory thalamus (**Figure 1**). Here, we performed recordings in awake mice to examine the effects of PV and SST neuron activation on the intact auditory circuit. We found that inactivating these distinct subpopulations of audTRN inhibitory neurons had diverging effects on auditory tone responses of MGB neurons **(Figure 2)**. While inactivation of PV^{TRN} neurons facilitated a large fraction of MGB neurons, we also found that inactivation of some PV^{TRN} and all SST^{TRN} neurons suppressed a large fraction of responses (**Figures 2, 3, 4**). Our results show that inactivation of both PV^{TRN} and SST^{TRN} neurons change the frequency tuning of MGB neurons **(Figure 5)**. In addition, computational models allowed us to identify several embedded variations of circuitry between TRN and MGB that could enable the experimental observations (**Figure 6**).

Together, our anatomical, electrophysiological, and simulation results indicate complex roles for TRN inhibition on MGB neurons and suggest a larger degree of divergence than what has been suggested from the anatomical work here and by others[42,43]. A variety of connection schemes have been proposed for TRN, including intra-TRN inhibition[58,58], lack of intra-TRN inhibition[57], typed reciprocal inhibition[42,43], and open-loop or divergent connectivity to thalamic nuclei[62,63]. Cross-modal TRN responses have been reported[64,65], offering further evidence of nuanced connectivity. In addition, gap junctions of the TRN could be exclusive within one set or both sets of cell types or modality, or promiscuous across types[45], or absent in adult tissue. Our computational survey of these possibilities suggests that divergence of TRN-MGB connectivity is necessary, in addition to reciprocal inhibition, to achieve the bidirectional responses in MGB observed for PV inactivation; and that some intra-TRN connectivity, whether gap junctional and/or GABAergic, plays a role in allowing for the suppressive effects of SST inactivation. Our modeling offers several predictions for future experiments, using optogenetic approaches. First, our model predicts a cell-specific inhibitory connection from SST^{TRN} to PV^{TRN}. Second,

divergent inhibition (*e.g.* from SST^{TRN} to vMGB neurons) could also be evaluated in the same experiment. Moreover, our modeling predicts that SST^{TRN} in that case are driven by higher order cells; thus inactivating the higher order population while also inactivating the SST^{TRN} would potentially reverse the observed impact on vMGB responses during SST silencing. Similar experiments in future studies could be applied to test a PV^{TRN}-d/mMGB connection.

One proposed mechanism for our results is the possibility of intra-TRN synapses between PV and SST neurons, similar to the interactions in cortical regions[1]. Evidence for GABAergic synapses between nearby TRN neurons in slice preparations is exceedingly sparse[57,66], but longer-range intra-TRN interactions are possible, and reports of dendro-dendritic synapses have been reported in the TRN of the cat[67]. We find an example of such a connection in slice recordings (**Supplementary Figure S8**). It has also been reported that excitatory collateral inputs from thalamic relay nuclei drive excitatory input onto TRN neurons and therefore activate TRN neurons[68]. It is also possible that the suppression effects in tone-responsive units of the MGB is a direct result of fast feedback arising from excitatory MGB collaterals, intra-TRN dendro-dendritic synapses, or other regions of GABAergic inputs to the TRN like the basal forebrain, substantia nigra or lateral hypothalamus[69–72].

The TRN receives diverse modulatory inputs, including projections from the substantia nigra reticulata[71], the basal forebrain[72–74], globus pallidus[75–77] and hypothalamus[70]. Whether these inputs are cell type-specific is unknown. Our results indicate that the impact of inhibiting or modulating specific TRN neuron types is complex and raises interest in the types, sources, and targets of modulatory input to the thalamocortical pathways, along with the function of these projections. For example, inhibition of TRN neurons that results in specific suppression or facilitation of the thalamocortical relay could be a mechanism for modulating sensory perception in line with behavioral state. Indeed, recent studies have shown the contributions of MGB to associative behavior memory tasks[78]. Whether and how disruption of inhibitory cell types of the TRN affects behavioral outputs of the MGB has yet to be explored. Our results suggest that PV^{TRN} and SST^{TRN} neurons may play distinct roles in behaviors that rely on lemniscal versus non-lemniscal thalamic function.

Our experiments and analyses do not account for the feedback provided to MGB and TRN from the cortex. Within the auditory thalamus, the TRN provides the majority of inhibition to the MGB, however, MGB neurons also receive feedback from corticothalamic neurons in L5/L6 of AC as well as input from other association areas, such as the BLA[33,79,80]. It is possible that the suppressive effects we observed included a component of fast feedback inhibition from another region of the brain, or polysynaptic interactions. Future studies using high-

density channel probes to record from multiple brain areas simultaneously could further our understanding of inhibitory circuit mechanisms. For example, recording from the TRN-MGB-AC circuit simultaneously while optogenetically manipulating 1) corticothalamic feedback, 2) TRN-MGB inhibitory synapses, or 3) collateral inputs from MGB to the TRN would allow recording effects of audTRN on neural responses along the auditory pathway. An extensive anatomical tracing study would also specifically identify possible sources of GABAergic input to PV and SST neurons involved in the auditory pathway. This could reveal possible sources of feedback inhibitory inputs to the TRN that might drive the tone-evoked suppression we observe in our study.

Combined, our results provide an insight into the complexity of the audTRN and identify cell-type specific mechanisms for controlling sound processing in the auditory thalamus.

RESOURCE AVAILABILITY

Lead Contact

Further information and requests for resources and reagents should be directed to and will be fulfilled by the Lead Contact, Maria Geffen (mgeffen@pennmedicine.upenn.edu).

Data & Code availability

Source data has been deposited in Dryad: https://doi.org/10.5061/dryad.ht76hdrq5. (Link for reviewers: https://datadryad.org/stash/share/7KOU8D8fZfH9cb7qoQeh103Tq4TSeNgftGf1nX7BQeo). Data analysis code is available on GitHub: https://github.com/geffenlab/Rolon_Martinez_2024. Code for the model is available at github: https://github.com/jhaaslab/TRN_MGB_celltypespecific.

Acknowledgements

The authors would like to thank the members of the Geffen and Haas laboratories and Yale Cohen for their discussions and helpful comments. This work was supported by the following grants from NIDCD: R01DC15527, R01DC014479, R03DC013660 to MNG, F31DC018473 to SRM, F31DC016524to CFA, from NINDS R01NS113241 to MNG and NIH R01 NS128713 to JSH.

REFERENCES

1. Blackwell, J.M., and Geffen, M.N. (2017). Progress and challenges for understanding the function of cortical microcircuits in auditory processing. Nat. Commun. *8*, 2165. https://doi.org/10.1038/s41467-017-01755-2.

2. Chen, Q.C., and Jen, P.H. (2000). Bicuculline application affects discharge patterns, rate-intensity functions, and frequency tuning characteristics of bat auditory cortical neurons. Hear. Res. *150*, 161–174. https://doi.org/10.1016/s0378-5955(00)00197-0.

3. Wu, G.K., Arbuckle, R., Liu, B.H., Tao, H.W., and Zhang, L.I. (2008). Lateral sharpening of cortical frequency tuning by approximately balanced inhibition. Neuron *58*, 132–143. https://doi.org/10.1016/j.neuron.2008.01.035.

4. Wang, J., Caspary, D., and Salvi, R.J. (2000). GABA-A antagonist causes dramatic expansion of tuning in primary auditory cortex. Neuroreport *11*, 1137–1140.

5. Pollak, G.D., Xie, R., Gittelman, J.X., Andoni, S., and Li, N. (2011). The dominance of inhibition in the inferior colliculus. Hear. Res. *274*, 27–39. https://doi.org/10.1016/j.heares.2010.05.010.

6. Myoga, M.H., Lehnert, S., Leibold, C., Felmy, F., and Grothe, B. (2014). Glycinergic inhibition tunes coincidence detection in the auditory brainstem. Nat. Commun. *5*, 3790. https://doi.org/10.1038/ncomms4790.

7. Burger, R.M., Fukui, I., Ohmori, H., and Rubel, E.W. (2011). Inhibition in the balance: binaurally coupled inhibitory feedback in sound localization circuitry. J. Neurophysiol. *106*, 4–14. https://doi.org/10.1152/jn.00205.2011.

8. Natan, R.G., Briguglio, J.J., Mwilambwe-Tshilobo, L., Jones, S.I., Aizenberg, M., Goldberg, E.M., and Geffen, M.N. (2015). Complementary control of sensory adaptation by two types of cortical interneurons. eLife *4*. https://doi.org/10.7554/eLife.09868.

9. Natan, R.G., Rao, W., and Geffen, M.N. (2017). Cortical Interneurons Differentially Shape Frequency Tuning following Adaptation. Cell Rep. *21*, 878–890. https://doi.org/10.1016/j.celrep.2017.10.012.

10. Aizenberg, M., Mwilambwe-Tshilobo, L., Briguglio, J.J., Natan, R.G., and Geffen, M.N. (2015). Bidirectional Regulation of Innate and Learned Behaviors That Rely on Frequency Discrimination by Cortical Inhibitory Neurons. PLoS Biol. *13*, 1–32. https://doi.org/10.1371/journal.pbio.1002308.

11. Briguglio, J.J., Aizenberg, M., Balasubramanian, V., and Geffen, M.N. (2018). Cortical neural activity predicts sensory acuity under optogenetic manipulation. J. Neurosci. *38*, 2094–2105. https://doi.org/10.1523/JNEUROSCI.2457-17.2017.

12. Park, Y., and Geffen, M.N. (2019). A Unifying Mechanistic Model of the Auditory Cortex with Inhibitory Subtypes. bioRxiv, 626358. https://doi.org/10.1101/626358.

13. Phillips, E.A., and Hasenstaub, A.R. (2016). Asymmetric effects of activating and inactivating cortical interneurons. eLife *5*. https://doi.org/10.7554/eLife.18383.

14. Phillips, E.A.K., Schreiner, C.E., and Hasenstaub, A.R. (2017). Cortical Interneurons Differentially Regulate the Effects of Acoustic Context. Cell Rep. *20*, 771–778. https://doi.org/10.1016/j.celrep.2017.07.001.

15. Moore, A.K., and Wehr, M. (2013). Parvalbumin-expressing inhibitory interneurons in auditory cortex are well-tuned for frequency. J. Neurosci. *33*, 13713–13723. https://doi.org/10.1523/JNEUROSCI.0663-13.2013.

16. Li, L.Y., Xiong, X.R., Ibrahim, L.A., Yuan, W., Tao, H.W., and Zhang, L.I. (2015). Differential Receptive Field Properties of Parvalbumin and Somatostatin Inhibitory Neurons in Mouse Auditory Cortex. Cereb. Cortex *25*, 1782–1791. https://doi.org/10.1093/cercor/bht417.

17. Hamilton, L.S., Sohl-Dickstein, J., Huth, A.G., Carels, V.M., Deisseroth, K., and Bao, S. (2013). Optogenetic Activation of an Inhibitory Network Enhances Feedforward Functional Connectivity in Auditory Cortex. Neuron *80*, 1066–1076. https://doi.org/10.1016/j.neuron.2013.08.017.

18. Seybold, B.A., Phillips, E.A.K., Schreiner, C.E., and Hasenstaub, A.R. (2015). Inhibitory Actions Unified by Network Integration. Neuron *87*, 1181–1192. https://doi.org/10.1016/J.NEURON.2015.09.013.

19. Ulanovsky, N., Las, L., and Nelken, I. (2003). Processing of low-probability sounds by cortical neurons. Nat. Neurosci. *6*, 391–398. https://doi.org/10.1038/nn1032.

20. Taaseh, N., Yaron, A., and Nelken, I. (2011). Stimulus-Specific Adaptation and Deviance Detection in the Rat Auditory Cortex. PLoS ONE *6*, e23369. https://doi.org/10.1371/journal.pone.0023369.

21. Fishman, Y.I., and Steinschneider, M. (2012). Searching for the mismatch negativity in primary auditory cortex of the awake monkey: Deviance detection or stimulus specific adaptation? J. Neurosci. *32*, 15747–15758. https://doi.org/10.1523/JNEUROSCI.2835-12.2012.

22. Farley, B.J., Quirk, M.C., Doherty, J.J., and Christian, E.P. (2010). Stimulus-Specific Adaptation in Auditory Cortex Is an NMDA-Independent Process Distinct from the Sensory Novelty Encoded by the Mismatch Negativity. J. Neurosci. *30*, 16475–16484. https://doi.org/10.1523/JNEUROSCI.2793-10.2010.

23. Polterovich, A., Jankowski, M.M., and Nelken, I. (2018). Deviance sensitivity in the auditory cortex of freely moving rats. PLoS ONE *13*, e0197678. https://doi.org/10.1371/journal.pone.0197678.

24. Bartlett, E.L. (2013). The organization and physiology of the auditory thalamus and its role in processing acoustic features important for speech perception. Brain Lang. *126*, 29–48. https://doi.org/10.1016/j.bandl.2013.03.003.

25. He, J. (2003). Corticofugal modulation of the auditory thalamus. Exp. Brain Res. *153*, 579–590. https://doi.org/10.1007/s00221-003-1680-5.

26. Crabtree, J.W. (1998). Organization in the auditory sector of the cat's thalamic reticular nucleus. J. Comp. Neurol. *390*, 167–182. https://doi.org/10.1002/(sici)1096-9861(19980112)390:2<167::aid-cne1>3.0.co;2-%23.

27. Crabtree, J.W. (2018). Functional diversity of thalamic reticular subnetworks. Front. Syst. Neurosci. *12*, 41. https://doi.org/10.3389/FNSYS.2018.00041/BIBTEX.

28. Houser, C.R., Vaughn, J.E., Barber, R.P., and Roberts, E. (1980). GABA neurons are the major cell type of the nucleus reticularis thalami. Brain Res. *200*, 341–354. https://doi.org/10.1016/0006-8993(80)90925-7.

29. Pinault, D. (2004). The thalamic reticular nucleus: structure, function and concept. Brain Res. Rev. *46*, 1–31. https://doi.org/10.1016/J.BRAINRESREV.2004.04.008.

30. Guillery, R.W., and Sherman, S.M. (2002). Thalamic relay functions and their role in corticocortical communication: generalizations from the visual system. Neuron *33*, 163–175.

31. Carroll, B.J., Sampathkumar, V., Kasthuri, N., and Sherman, S.M. (2022). Layer 5 of cortex innervates the thalamic reticular nucleus in mice. Proc. Natl. Acad. Sci. U. S. A. *119*. https://doi.org/10.1073/PNAS.2205209119.

32. Gentet, L.J., and Ulrich, D. (2004). Electrophysiological characterization of synaptic connections between layer VI cortical cells and neurons of the nucleus reticularis thalami in juvenile rats. Eur. J. Neurosci. *19*, 625–633. https://doi.org/10.1111/j.1460-9568.2004.03168.x.

33. Guo, W., Clause, A.R., Barth-Maron, A., and Polley, D.B. (2017). A Corticothalamic Circuit for Dynamic Switching between Feature Detection and Discrimination. Neuron *95*, 180-194.e5. https://doi.org/10.1016/j.neuron.2017.05.019.

34. Lam, Y.W., and Sherman, S.M. (2005). Mapping by laser photostimulation of connections between the thalamic reticular and ventral posterior lateral nuclei in the rat. J. Neurophysiol. *94*, 2472–2483. https://doi.org/10.1152/jn.00206.2005.

35. Lam, Y.W., and Sherman, S.M. (2011). Functional organization of the thalamic input to the thalamic reticular nucleus. J. Neurosci. *31*, 6791–6799. https://doi.org/10.1523/JNEUROSCI.3073-10.2011.

36. Ahrens, S., Jaramillo, S., Yu, K., Ghosh, S., Hwang, G.R., Paik, R., Lai, C., He, M., Huang, Z.J., and Li, B. (2015). ErbB4 regulation of a thalamic reticular nucleus circuit for sensory selection. Nat. Neurosci. *18*, 104–111. https://doi.org/10.1038/nn.3897.

37. Crick, F. (2006). Function of the thalamic reticular complex: the searchlight hypothesis. Proc. Natl. Acad. Sci. *81*, 4586–4590. https://doi.org/10.1073/pnas.81.14.4586.

38. Halassa, M.M., Chen, Z., Wimmer, R.D., Brunetti, P.M., Zhao, S., Zikopoulos, B., Wang, F., Brown, E.N., and Wilson, M.A. (2014). State-dependent architecture of thalamic reticular subnetworks. Cell *158*, 808–821. https://doi.org/10.1016/j.cell.2014.06.025.

39. Nakajima, M., Schmitt, L.I., and Halassa, M.M. (2019). Prefrontal Cortex Regulates Sensory Filtering through a Basal Ganglia-to-Thalamus Pathway. Neuron *103*, 445-458.e10. https://doi.org/10.1016/j.neuron.2019.05.026.

40. Schmitt, L.I., Wimmer, R.D., Nakajima, M., Happ, M., Mofakham, S., and Halassa, M.M. (2017). Thalamic amplification of cortical connectivity sustains attentional control. Nature *545*, 219–223. https://doi.org/10.1038/nature22073.

41. Wimmer, R.D., Schmitt, L.I., Davidson, T.J., Nakajima, M., Deisseroth, K., and Halassa, M.M. (2015). Thalamic control of sensory selection in divided attention. Nature *526*, 705–709. https://doi.org/10.1038/nature15398.

42. Martinez-Garcia, R.I., Voelcker, B., Zaltsman, J.B., Patrick, S.L., Stevens, T.R., Connors, B.W., Cruikshank, S.J., and Carney, N.D. (2020). Two dynamically distinct circuits drive inhibition in the sensory thalamus. Nature *583*. https://doi.org/10.1038/s41586-020-2512-5.

43. Clemente-Perez, A., Makinson, S.R., Higashikubo, B., Brovarney, S., Cho, F.S., Urry, A., Holden, S.S., Wimer, M., Dávid, C., Fenno, L.E., et al. (2017). Distinct Thalamic Reticular Cell Types Differentially Modulate Normal and Pathological Cortical Rhythms. Cell Rep. *19*, 2130–2142. https://doi.org/10.1016/j.celrep.2017.05.044.

44. Li, Y., Lopez-Huerta, V.G., Adiconis, X., Levandowski, K., Choi, S., Simmons, S.K., Arias-Garcia, M.A., Guo, B., Yao, A.Y., Blosser, T.R., et al. (2020). Distinct subnetworks of the thalamic reticular nucleus. Nature *583*. https://doi.org/10.1038/s41586-020-2504-5.

45. Vaughn, M.J., Laswick, Z., Wang, H., and Haas, J.S. (2024). Functionally Distinct Circuits Are Linked by Heterocellular Electrical Synapses in the Thalamic Reticular Nucleus. eNeuro *11*. https://doi.org/10.1523/ENEURO.0269-23.2023.

46. Johnson, K.R., Tian, C., Gagnon, L.H., Jiang, H., Ding, D., and Salvi, R. (2017). Effects of Cdh23 single nucleotide substitutions on age-related hearing loss in C57BL/6 and 129S1/Sv mice and comparisons with congenic strains. Sci. Rep. *7*, 44450. https://doi.org/10.1038/srep44450.

47. Siegle, J.H., López, A.C., Patel, Y.A., Abramov, K., Ohayon, S., and Voigts, J. (2017). Open Ephys: an open-source, plugin-based platform for multichannel electrophysiology. J. Neural Eng. *14*, 045003. https://doi.org/10.1088/1741-2552/aa5eea.

48. Pachitariu, M., Sridhar, S., and Stringer, C. (2023). Solving the spike sorting problem with Kilosort. Preprint at bioRxiv, https://doi.org/10.1101/2023.01.07.523036 https://doi.org/10.1101/2023.01.07.523036.

49. Stringer, C., Wang, T., Michaelos, M., and Pachitariu, M. (2021). Cellpose: a generalist algorithm for cellular segmentation. Nat. Methods *18*, 100–106. https://doi.org/10.1038/s41592-020-01018-x.

50. Destexhe, A., Bal, T., McCormick, D.A., and Sejnowski, T.J. (1996). Ionic mechanisms underlying synchronized oscillations and propagating waves in a model of ferret thalamic slices. J. Neurophysiol. *76*, 2049–2070. https://doi.org/10.1152/jn.1996.76.3.2049.

51. Pham, T., and Haas, J.S. (2018). Electrical synapses between inhibitory neurons shape the responses of principal neurons to transient inputs in the thalamus: a modeling study. Sci. Rep. *8*, 7763. https://doi.org/10.1038/s41598-018-25956-x.

52. Traub, R.D., Contreras, D., Cunningham, M.O., Murray, H., LeBeau, F.E.N., Roopun, A., Bibbig, A., Wilent, W.B., Higley, M.J., and Whittington, M.A. (2005). Single-Column Thalamocortical Network Model Exhibiting Gamma Oscillations, Sleep Spindles, and Epileptogenic Bursts. J. Neurophysiol. *93*, 2194–2232. https://doi.org/10.1152/jn.00983.2004.

53. Desai, N.V., and Varela, C. (2021). Distinct burst properties contribute to the functional diversity of thalamic nuclei. J. Comp. Neurol. *529*, 3726–3750. https://doi.org/10.1002/cne.25141.

54. Lu, E., Llano, D.A., and Sherman, S.M. (2009). Different distributions of calbindin and calretinin immunostaining across the medial and dorsal divisions of the mouse medial geniculate body. Hear. Res. *257*, 16–23. https://doi.org/10.1016/J.HEARES.2009.07.009.

55. Mahn, M., Gibor, L., Patil, P., Cohen-Kashi Malina, K., Oring, S., Printz, Y., Levy, R., Lampl, I., and Yizhar, O. (2018). High-efficiency optogenetic silencing with soma-targeted anion-conducting channelrhodopsins. Nat. Commun. *9*, 4125. https://doi.org/10.1038/s41467-018-06511-8.

56. Pham, T., and Haas, J.S. (2019). Electrical synapses regulate both subthreshold integration and population activity of principal cells in response to transient inputs within canonical feedforward circuits. PLOS Comput. Biol. *15*, e1006440. https://doi.org/10.1371/journal.pcbi.1006440.

57. Hou, G., Smith, A.G., and Zhang, Z.-W. (2016). Lack of intrinsic GABAergic connections in the thalamic reticular nucleus of the mouse. J. Neurosci. *36*, 7246–7252.

58. Deleuze, C., and Huguenard, J.R. (2006). Distinct Electrical and Chemical Connectivity Maps in the Thalamic Reticular Nucleus: Potential Roles in Synchronization and Sensation. J. Neurosci. *26*, 8633–8645. https://doi.org/10.1523/JNEUROSCI.2333-06.2006.

59. Lam, Y.-W., Nelson, C.S., and Sherman, S.M. (2006). Mapping of the Functional Interconnections Between Thalamic Reticular Neurons Using Photostimulation. J. Neurophysiol. *96*, 2593–2600. https://doi.org/10.1152/jn.00555.2006.

60. Pinault, D., and Deschênes, M. (1998). Projection and innervation patterns of individual thalamic reticular axons in the thalamus of the adult rat: A three-dimensional, graphic, and morphometric analysis. J. Comp. Neurol. *391*, 180–203. https://doi.org/10.1002/(SICI)1096-9861(19980209)391:2<180::AID-CNE3>3.0.CO;2-Z.

61. Shosaku, A., Kayama, Y., Sumitomo, I., Sugitani, M., and Iwama, K. (1989). Analysis of recurrent inhibitory circuit in rat thalamus: Neurophysiology of the thalamic reticular nucleus. Prog. Neurobiol. *32*, 77–102. https://doi.org/10.1016/0301-0082(89)90011-7.

62. Crabtree, J.W., Collingridge, G.L., and Isaac, J.T.R. (1998). A new intrathalamic pathway linking modality-related nuclei in the dorsal thalamus. Nat. Neurosci. *1*, 389–394. https://doi.org/10.1038/1603.

63. Crabtree, J.W., and Isaac, J.T.R. (2002). New Intrathalamic Pathways Allowing Modality-Related and Cross-Modality Switching in the Dorsal Thalamus. J. Neurosci. *22*, 8754–8761. https://doi.org/10.1523/JNEUROSCI.22-19-08754.2002.

64. Kimura, A. (2014). Diverse subthreshold cross-modal sensory interactions in the thalamic reticular nucleus: implications for new pathways of cross-modal attentional gating function. Eur J Neurosci *39*, 1405–1418.

65. Kimura, A. (2024). Cross-modal sensitivities to auditory and visual stimulations in the first-order somatosensory thalamic nucleus. Eur. J. Neurosci. *60*, 5621–5657. https://doi.org/10.1111/ejn.16510.

66. Landisman, C.E., and Coulon, P. (2024). A Mixed Electrical and Chemical Synapse in the Thalamic Reticular Nucleus. J. Neurophysiol. https://doi.org/10.1152/jn.00339.2024.

67. Desche^nes, M., Madariaga-Domich, A., and Steriade, M. (1985). Dendrodendritic synapses in the cat reticularis thalami nucleus: a structural basis for thalamic spindle synchronization. Brain Res. *334*, 165–168. https://doi.org/10.1016/0006-8993(85)90580-3.

68. Yen, C.T., Conley, M., Hendry, S.H., and Jones, E.G. (1985). The morphology of physiologically identified GABAergic neurons in the somatic sensory part of the thalamic reticular nucleus in the cat. J. Neurosci. Off. J. Soc. Neurosci. *5*, 2254–2268. https://doi.org/10.1523/JNEUROSCI.05-08-02254.1985.

69. Asanuma, C., and Porter, L.L. (1990). Light and electron microscopic evidence for a GABAergic projection from the caudal basal forebrain to the thalamic reticular nucleus in rats. J. Comp. Neurol. *302*, 159–172. https://doi.org/10.1002/cne.903020112.

70. Herrera, C.G., Cadavieco, M.C., Jego, S., Ponomarenko, A., Korotkova, T., and Adamantidis, A. (2015). Hypothalamic feedforward inhibition of thalamocortical network controls arousal and consciousness. Nat. Neurosci. *19*, 290–298. https://doi.org/10.1038/nn.4209.

71. Paré, D., Hazrati, L.N., Parent, A., and Steriade, M. (1990). Substantia nigra pars reticulata projects to the reticular thalamic nucleus of the cat: a morphological and electrophysiological study. Brain Res. *535*, 139–146. https://doi.org/10.1016/0006-8993(90)91832-2.

72. Asanuma, C. (1989). Axonal arborizations of a magnocellular basal nucleus input and their relation to the neurons in the thalamic reticular nucleus of rats. Proc. Natl. Acad. Sci. *86*, 4746–4750. https://doi.org/10.1073/pnas.86.12.4746.

73. Jourdain, A., Semba, K., and Fibiger, H.C. (1989). Basal forebrain and mesopontine tegmental projections to the reticular thalamic nucleus: an axonal collateralization and immunohistochemical study in the rat. Brain Res *505*, 55–65. https://doi.org/10.1016/0006-8993(89)90115-7.

74. Bickford, M.E., Gunluk, A.E., Van Horn, S.C., and Sherman, S.M. (1994). GABAergic projection from the basal forebrain to the visual sector of the thalamic reticular nucleus in the cat. J Comp Neurol *348*, 481–510. https://doi.org/10.1002/cne.903480402.

75. Gandia, J.A., De Las Heras, S., Garcia, M., and Gimenez-Amaya, J.M. (1993). Afferent projections to the reticular thalamic nucleus from the globus pallidus and the substantia nigra in the rat. Brain Res Bull *32*, 351–358. https://doi.org/10.1016/0361-9230(93)90199-l.

76. Halassa, M.M., and Acsady, L. (2016). Thalamic Inhibition: Diverse Sources, Diverse Scales. Trends Neurosci *39*, 680–693. https://doi.org/10.1016/j.tins.2016.08.001.

77. Cornwall, J., Cooper, J.D., and Phillipson, O.T. (1990). Projections to the rostral reticular thalamic nucleus in the rat. Exp Brain Res *80*, 157–171. https://doi.org/10.1007/bf00228857.

78. Belén Pardi, M., Vogenstahl, J., Dalmay, T., Spanò, T., Pu, D.L., Naumann, L.B., Kretschmer, F., Sprekeler, H., and Letzkus, J.J. (2020). A thalamocortical top-down circuit for associative memory. Science *370*, 844–848. https://doi.org/10.1126/SCIENCE.ABC2399/SUPPL_FILE/ABC2399_PARDI_SM.PDF.

79. Lee, C.C., and Sherman, S.M. (2010). Drivers and Modulators in the Central Auditory Pathways. Front. Neurosci. *4*, 79. https://doi.org/10.3389/neuro.01.014.2010.

80. Winer, J.A. (2005). Decoding the auditory corticofugal systems. Hear. Res. *207*, 1–9. https://doi.org/10.1016/j.heares.2005.06.007.

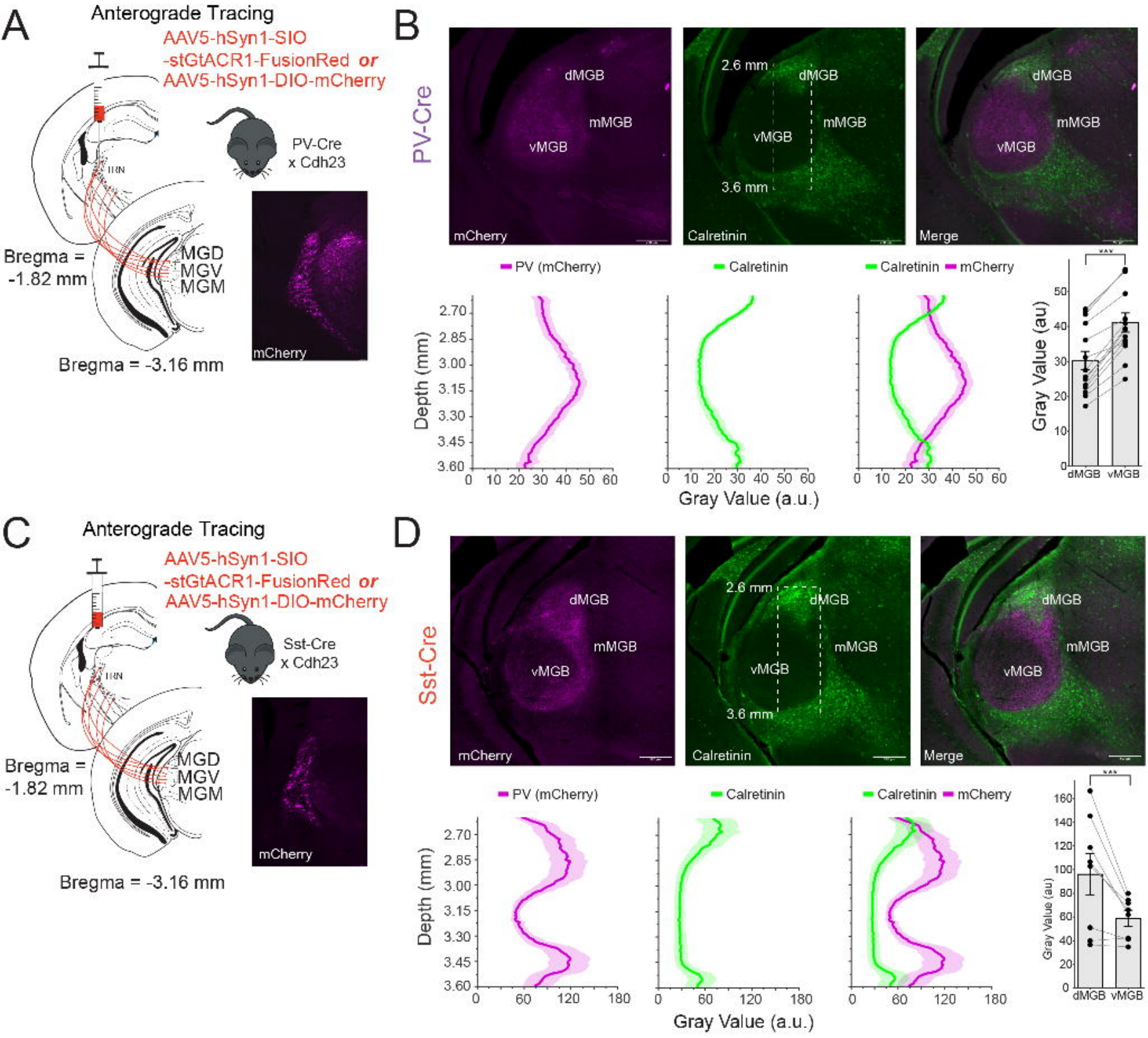
A
Anterograde Tracing
AAV5-hSyn1-SIO
-stGtACR1-FusionRed or
AAV5-hSyn1-DIO-mCherry
PV-Cre
x Cdh23
Bregma =
-1.82 mm
MGD
MGV
MGM
mCherry
Bregma = -3.16 mm
B
PV-Cre
dMGB
mMGB
vMGB
mCherry
2.6 mm
3.6 mm
Calretinin
Merge
PV (mCherry)
Calretinin
Calretinin mCherry
Depth (mm)
Gray Value (a.u.)
Gray Value (au)
C
Anterograde Tracing
AAV5-hSyn1-SIO
-stGtACR1-FusionRed or
AAV5-hSyn1-DIO-mCherry
Sst-Cre
x Cdh23
Bregma =
-1.82 mm
MGD
MGV
MGM
mCherry
Bregma = -3.16 mm
D
Sst-Cre
dMGB
mMGB
vMGB
mCherry
2.6 mm
3.6 mm
Calretinin
Merge
PV (mCherry)
Calretinin
Calretinin mCherry
Depth (mm)
Gray Value (a.u.)
Gray Value (au)

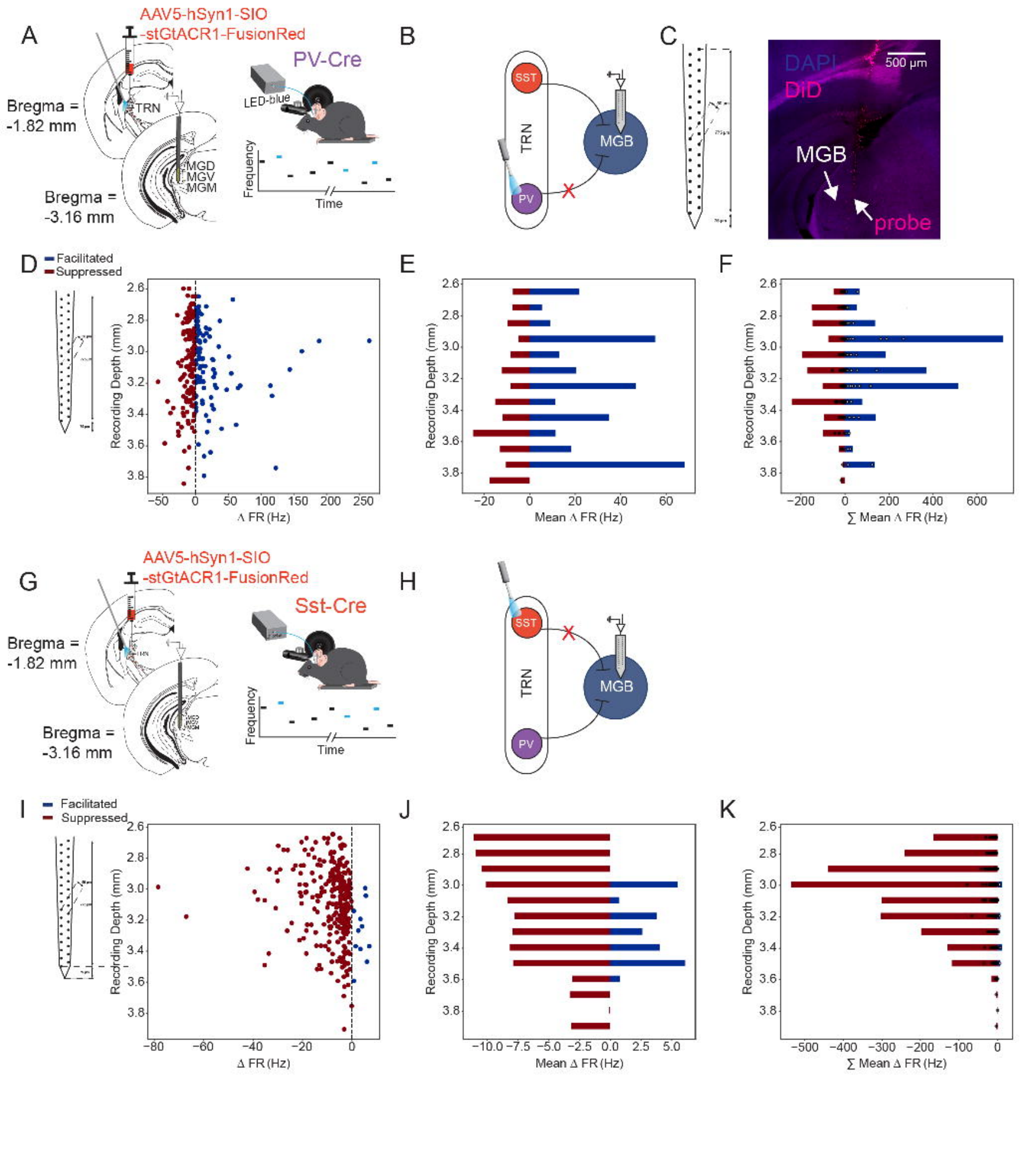
A
AAV5-hSyn1-SIO
-stGtACR1-FusionRed
PV-Cre
Bregma =
-1.82 mm
TRN
LED-blue
Frequency
Time
MGD
MGV
MGM
Bregma =
-3.16 mm
B
SST
TRN
MGB
PV
C
DAPI
DiD
500 µm
MGB
probe
D
Facilitated
Suppressed
Recording Depth (mm)
Δ FR (Hz)
E
Recording Depth (mm)
Mean Δ FR (Hz)
F
Recording Depth (mm)
∑ Mean Δ FR (Hz)
G
AAV5-hSyn1-SIO
-stGtACR1-FusionRed
Sst-Cre
Bregma =
-1.82 mm
Frequency
Time
Bregma =
-3.16 mm
H
SST
TRN
MGB
PV
I
Facilitated
Suppressed
Recording Depth (mm)
Δ FR (Hz)
J
Recording Depth (mm)
Mean Δ FR (Hz)
K
Recording Depth (mm)
∑ Mean Δ FR (Hz)

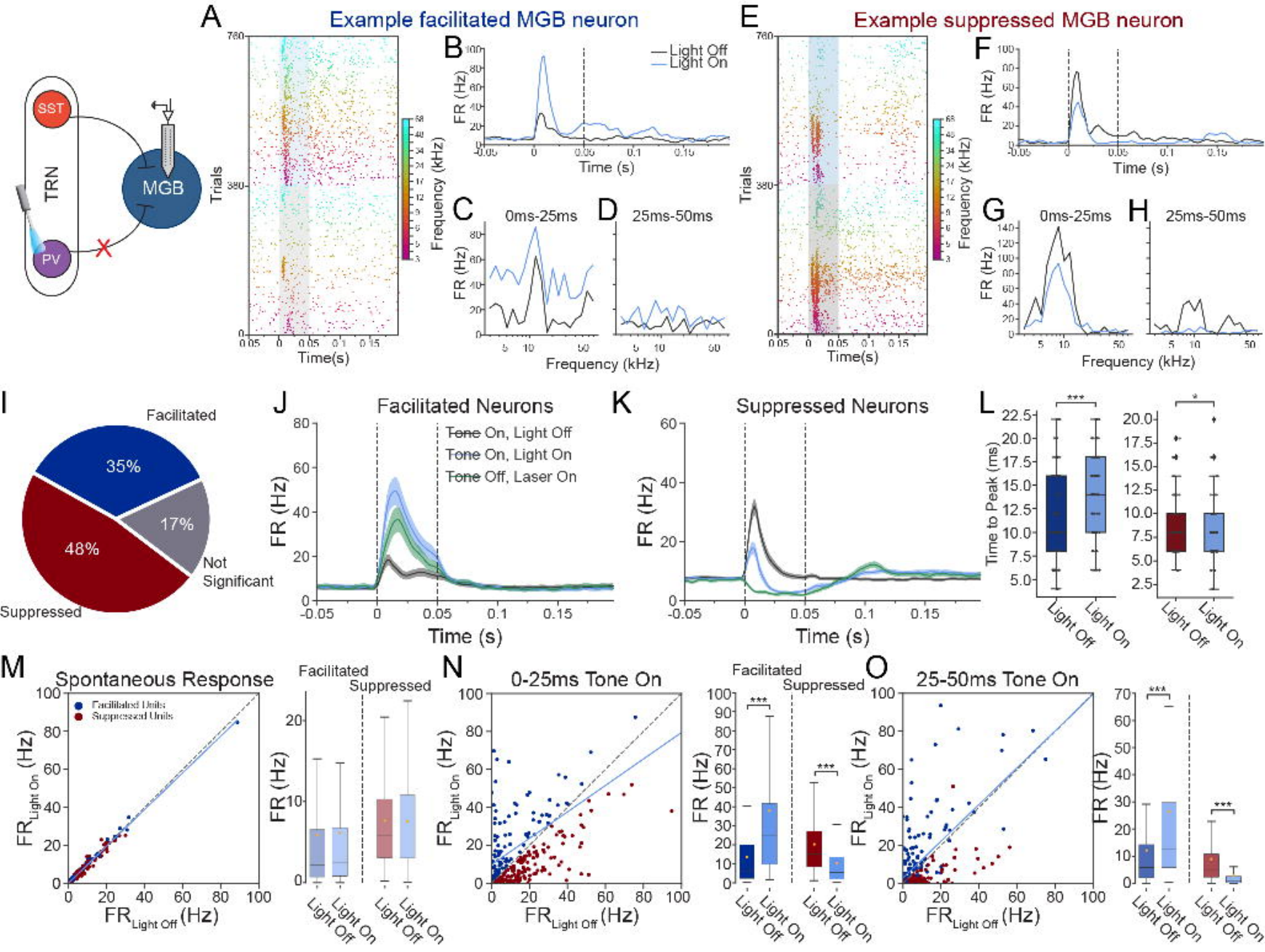
A
Example facilitated MGB neuron
SST
TRN
MGB
PV
Trials
Time(s)
Frequency (kHz)
B
Light Off
Light On
FR (Hz)
Time (s)
C
0ms-25ms
D
25ms-50ms
Frequency (kHz)
E
Example suppressed MGB neuron
F
G
H
I
Facilitated
35%
17%
48%
Not Significant
Suppressed
J
Facilitated Neurons
Tone On, Light Off
Tone On, Light On
Tone Off, Laser On
K
Suppressed Neurons
L
Time to Peak (ms)
Light Off
Light On
M
Spontaneous Response
Facilitated Units
Suppressed Units
Facilitated
Suppressed
N
0-25ms Tone On
O
25-50ms Tone On

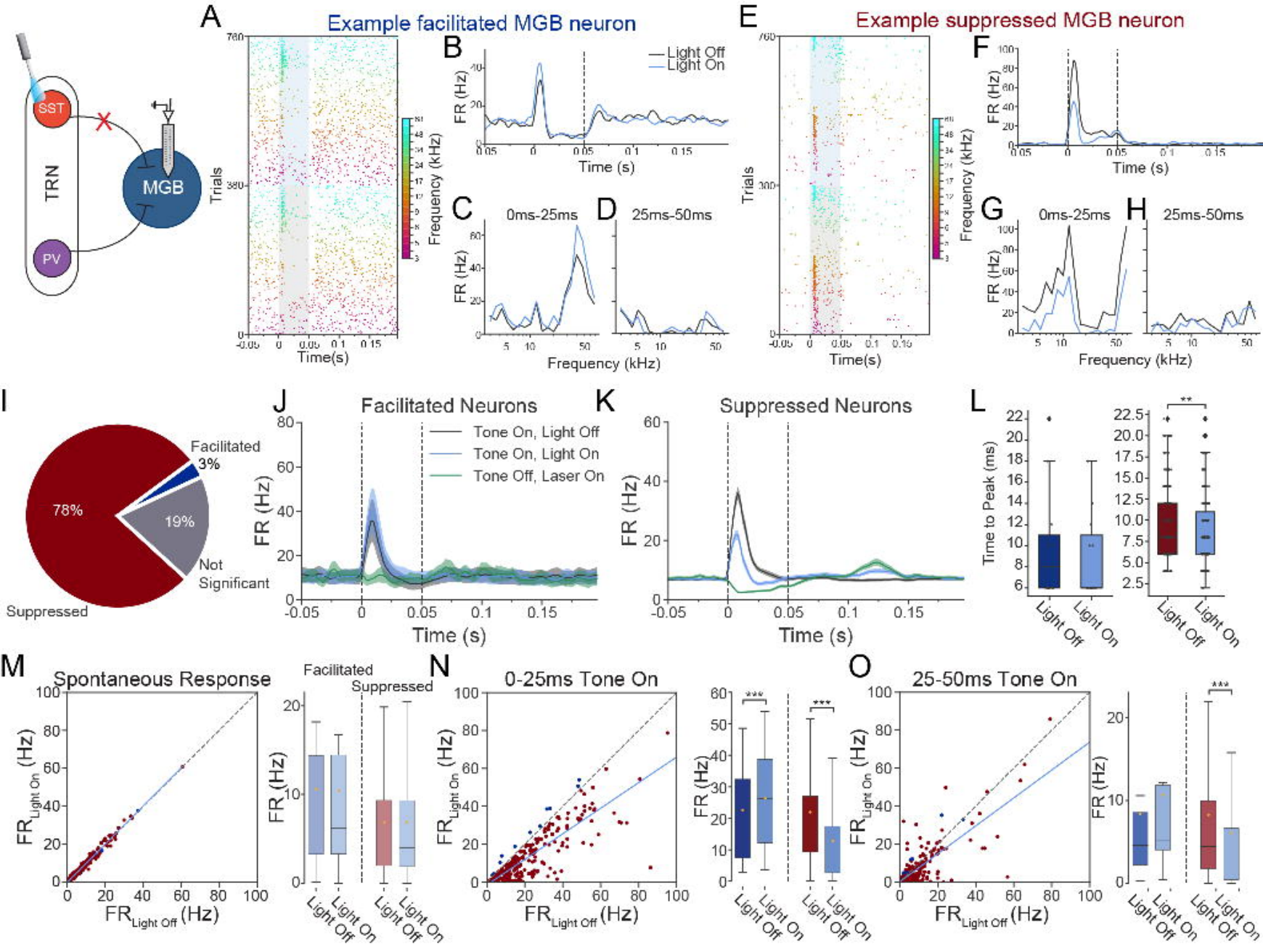
A
Example facilitated MGB neuron
SST
TRN
PV
MGB
Trials
Time(s)
Frequency (kHz)
B
Light Off
Light On
FR (Hz)
Time (s)
C
0ms-25ms
D
25ms-50ms
Frequency (kHz)
E
Example suppressed MGB neuron
F
G
H
I
Facilitated
3%
78%
19%
Not Significant
Suppressed
J
Facilitated Neurons
Tone On, Light Off
Tone On, Light On
Tone Off, Laser On
K
Suppressed Neurons
L
Time to Peak (ms)
Light Off
Light On
M
Spontaneous Response
Facilitated
Suppressed
N
0-25ms Tone On
O
25-50ms Tone On

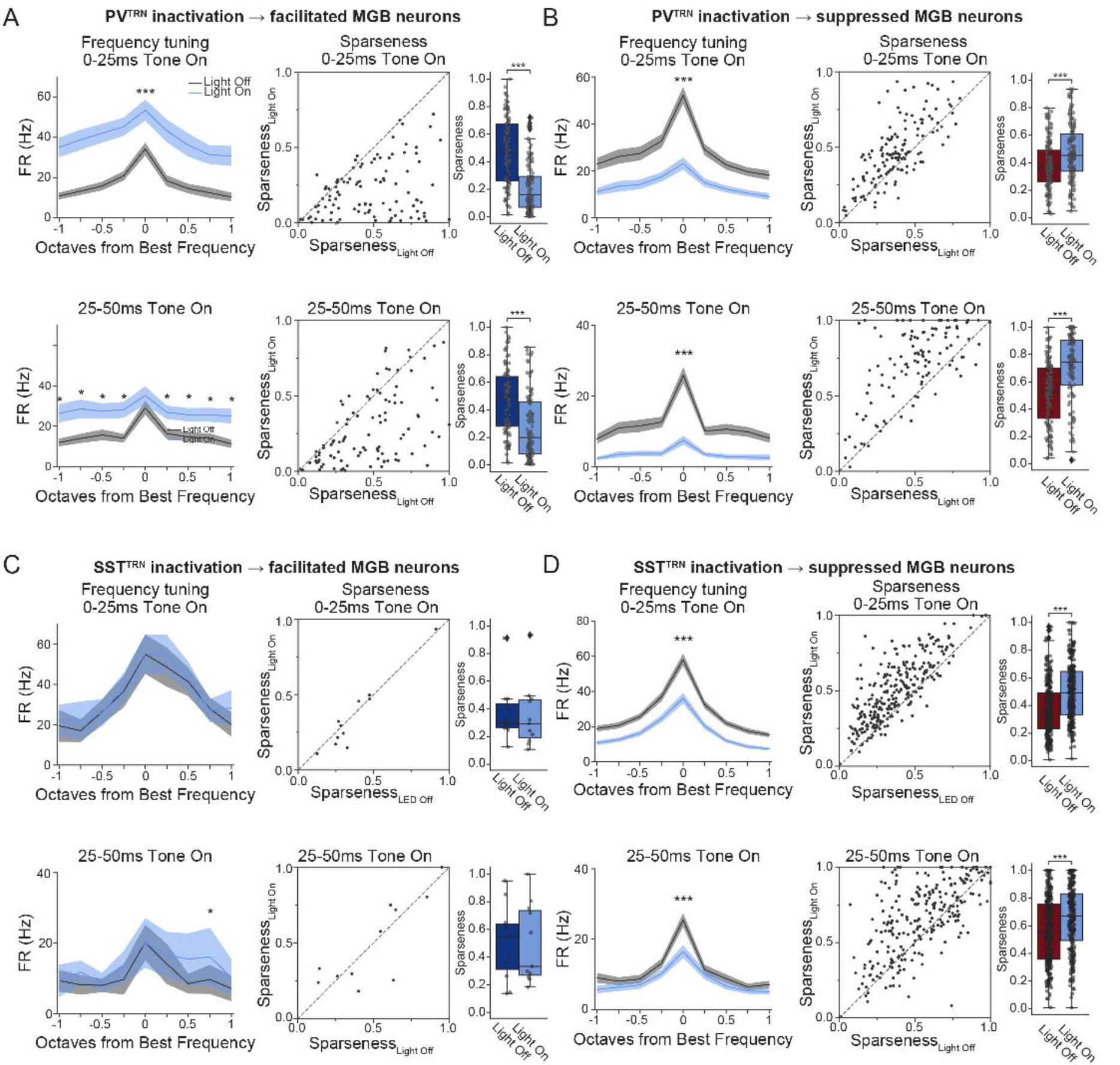
A
PV^TRN inactivation → facilitated MGB neurons
Frequency tuning
0-25ms Tone On
Light Off
Light On
FR (Hz)
Octaves from Best Frequency
Sparseness
0-25ms Tone On
Sparseness_Light On
Sparseness_Light Off
Sparseness
Light Off
Light On
25-50ms Tone On
B
PV^TRN inactivation → suppressed MGB neurons
C
SST^TRN inactivation → facilitated MGB neurons
Sparseness_LED Off
D
SST^TRN inactivation → suppressed MGB neurons